# PDA Measurements in a Three-Phase Bubble Column

**Z. W. Gan**
Division of Environmental and Water resources Engineering, School of Civil and Environmental Engineering, Nanyang Technological University, Singapore 639798

**S. C. M. Yu**
Division of Aerospace Engineering, School of Mechanical and Aerospace Engineering, Nanyang Technological University, Singapore 639798

**A. W. K. Law**
Division of Environmental and Water resources Engineering, School of Civil and Environmental Engineering, Nanyang Technological University, Singapore 639798

*DOI 10.1002/aic.14041*
*Published online February 25, 2013 in Wiley Online Library (wileyonlinelibrary.com)*

*Phase Doppler anemometry was used to quantify the flow characteristic of a three phases (liquid, solid, and bubbles) cylindrical bubble column driven by a point air source made of a 30-mm diameter perforated air stone centrally mounted at the bottom. The cylindrical bubble column had an inner diameter of 152 mm and was filled with liquid up to 1 m above the point source. Acrylic beads with a nominal diameter of 3 mm were used as the solid phase. To match the density of the solid phase which was 1.05 kg/m$^3$, the liquid density was raised to about 1.0485 kg/m3 by added salt. The bubble diameters generated were within the range of 600–2400 μm. The detailed turbulent characteristics of the liquid-phase velocity, bubble diameter, bubble velocity, and solid velocity were measured at three different air rates, namely 0.4, 0.8, and 1.2 L/min (corresponding to average gas volume fraction of 0.0084, 0.0168, and 0.0258, respectively) for the homogeneous bubble column regime. With the addition of the solid phase, the flow field was found to be relatively steady compared to the two-phase column referencing the probability density functions for both the liquid and bubble velocities. An analysis based on the determination of the drag forces and transversal lift forces was performed to examine the flow stability in the three-phase bubble column. The analysis illustrated that how the added solid phase effectively stabilized the flow field to achieve a steady circulation in the bubble column and a generalized criterion for the flow stability in the three-phase bubble column was derived. Further investigation for the transition and the heterogeneous bubble column regime with air rates at 2.0 and 4.0 L/min shown that this criterion can also be used as a general prediction of flow stability in this three-phase bubble column.* © 2013 American Institute of Chemical Engineers *AIChE J*, 59: 2286–2307, 2013
*Keywords: bubble columns, multiphase flow, hydrodynamics, stability, phase Doppler anemometry, lift force*

## Introduction

Bubble columns are multiphase flow mixers in which a gas or a mixture of gases is introduced and rises in form of bubbles continuously through a liquid phase. Due largely to the simplicity of operation, absence of moving parts, low operating costs as well as easily adjusted liquid residence time, bubble columns are widely used in the industry for chemical, biochemical, and petrochemical processing.[1,2] From an engineering application point of view, controllable hydrodynamic shear forces for both the bubble and solid phase are desirable so as to enhance the efficiency of the microbial granulation process. The hydrodynamics of gas–liquid and gas–liquid–solid systems have been extensively studied over the past few decades.[3–8]

It is well-known that the behavior of the bubble column reactor is hard to predict due to the complex interactions among the three phases. There have been many types of scale-up model studies based on the measurements of the time-averaged data in the flow field. Several nondimensional numbers and empirical models, such as those proposed by Groen et al.[9] and Yang et al.,[10] had also been put forward. However, there remains insufficient detailed physical understanding and predictive tools for the design and optimization of such systems. For example, the transient flow structure of some bubble columns have exhibited unstable behaviors such as the bubble swarm meandering, which have not been fully understood.[11]

In multiphase bubble columns, the bubble and solid phases exist as a dispersed phase in the continuous liquid phase. Depending on the nature of dispersion, the gas–liquid mixture moves in one of the two characteristic regimes, which are known as homogeneous and heterogeneous regimes.[12] The homogeneous regime implies a uniform gas distribution with the bubbles rising almost vertically inside the column. The carried up liquid by the bubbles must, however, return downward in some regions to achieve a zero net liquid flow

Correspondence concerning this article should be addressed to Z. W. Gan at ganz0004@e.ntu.edu.sg.

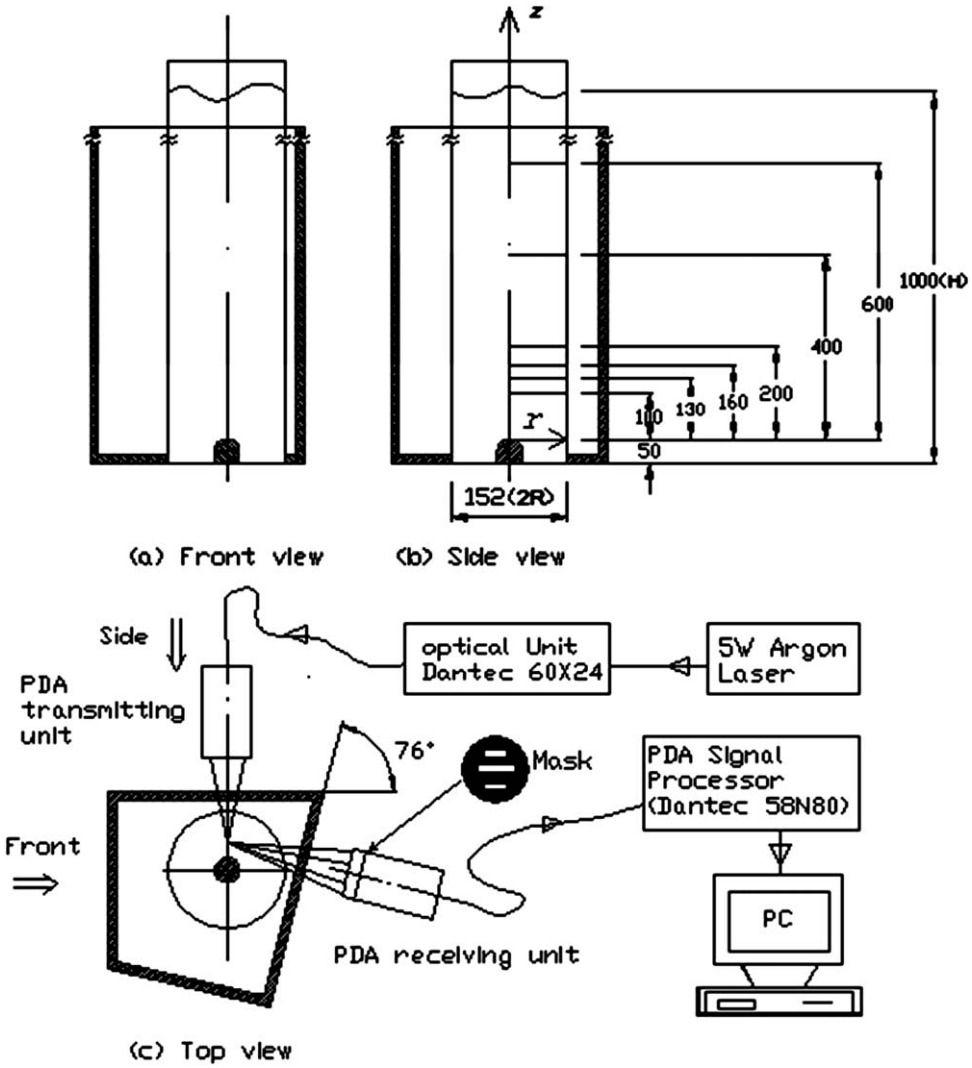


**Figure 1. Schematic of the bubble column and the Fiber PDA system, (all dimensions in mm).**

in the column. In the heterogeneous regime, most of the ascending bubbles are centralized in a small area. Large-scale and strong nonuniformities in buoyancy distribution drive large-scale and strong convective motion of liquid and bubbles inside the bubble column.

In recent years, the technique of phase Doppler anemometry (PDA) had been successfully applied to many complex two-phase flow environments with spherical particles such as liquid droplet flow,[13] paint spray,[14] and plasma spray.[15] Braeske et al.[16] was among the first to measure the size, velocity, and holdup of bubble and solid phases in the three-phase fluidized beds using PDA. Lain et al.[17] presented a numerical study with the extension of an Euler/Lagrange approach to allow the time-dependent calculations of bubbly flows, and validated the results of the numerical calculations based on PDA measurements. Brenn et al.[18] investigated the two-phase flow characteristics of a bubble column with PDA. They discovered that at most locations in the flow field, the time average velocity probability density functions of bubbles and liquid can be described by two superimposed Gaussian functions, and the bubbles belonging to the two Gaussians exhibited different slip velocities with the liquid phase. Brenn et al.[18] attributed the Gaussian function with the lower mean velocity to the downward motion of the liquid phase, and that of the higher mean velocity to the upward motion of the bubbles. The presence of the two Gaussion distributions can have an important effect to the overall stability of the bubble column. Warsito and Fan[11] developed a three-dimensional (3-D) method, named electrical capacitance tomography imaging based on a neural-network multicriterion optimization, to determine the flow structure of the bubble plume motion. They concluded that the liquid vortices in the vortical-spiral liquid region are of rounded shapes existing in cells or pockets which are disconnected from each other and disappear faster at a higher gas velocity or in the presence of solid particles in gas–liquid–solid systems. In our previous work,[19] PDA was used to obtain the dynamic information of the air and liquid-phase velocities as well as the bubble sizes in a model air-liquid two-phase bubble column. The results revealed that at all positions in the model two-phase bubble column, the velocity for both bubble and liquid phases can be resolved into a combination of a higher Gaussian and a lower Gaussian distribution similar to Brenn et al.[18] A stability criterion was then proposed based on the bimodal characteristics as well as the consideration of the interplay between the effect of the drag and lift on the bubble swarm inside the bubble column. By considering the disturbance length scale to be the

bubble size, it was found that the criterion was able to predict the overall flow behavior inside the column, as well as the transition from an unsteady to a steady flow pattern along the column height.

This study aims to investigate the flow dynamics of a three-phase bubble column driven by a bottom centrally mounted point air source. There are two objectives for this three-phase investigation. First, the use of a bottom point air source to drive a three-phase bubble column is very common in the environmental industry. It is, therefore, necessary to investigate the characteristics of this kind of bubble generator for possible improvement for environmental applications. Second, the stability criterion for the flow circulation inside a multiphase bubble column has not been fully resolved. The point source configuration here would create spatial contrasts in the bubble concentration and flow gradients. The stability at different locations inside the column can be examined with fine resolutions using the detailed and accurate measurements of all the three phases. A better picture of the three-phase flow field can then be depicted in the model bubble column. With the dynamical characteristics of all the three phases from PDA measurements, the drag coefficient $C_D$and lift coefficient$C_L$, which are well-known to have an important influence to the stability of the flow field in the bubble column,[4] can also be quantified. Finally, the influence to the stability of bubbly flow from the solid phase can be examined.

This article is arranged in four parts. Following the introduction, the experimental set-up will be first described. After that, the results for the model three-phase bubble column are presented. The article ends with a summary of important concluding remarks.

## Experimental Arrangement and Experiments

### *Bubble column*

The experiments were conducted in a vertical bubble column shown schematically in Figure 1. The bubble column had an internal diameter ($D$) of 152 mm. Filtrated water with added soap and salt was chosen as the liquid phase. The decreased surface tension led to smaller bubbles that were more spherical and hence beneficial to the PDA measurements. The liquid was filled up to a level of 1000 mm from the bottom, which was equivalent to a height ($H$) of 950 mm above the tip of the air stone. Thus, the aspect ratio was about H/D = 6.3.

With the cylindrical cross-section, refractive index matching was necessary to avoid the refraction of the laser light at the curved walls of the column. To achieve the matching, a special material of fluorinated ethylene–propylene polymer (FEP) was chosen as the column walls. FEP is a kind of Teflon with a refractive index ($m = 1.338$) very close to the liquid in our investigation ($m = 1.336$) and with a light transmittance of 95%. An observation box with plane glass windows was also constructed around the column and filled with filtrated water. The windows were arranged in the way that the optical axes of the PDA transmitting and receiving units are normal to the glass walls.

A perforated air stone with 30-cm diameter was used to introduce dry air into the flow from the center of the bottom of the column. This type of point air source is very commonly used in the environmental industry (e.g., for wastewater treatment) due to its simplicity, low cost, high-air flux, and easy control.[20,21] Photo taken with a CCD camera in Figure 2a showed that the bubbles generated by the stone were essentially spherical, with a size range of about 600–2400 $\mu$m. Measurements at different air flow rates also showed that the bubble size had a normal distribution with a peak near 1.5 mm.

The count distribution of the bubble and solid phases at the air flow rate of 0.4 L/min at $r = 0$ and $z = 100$ mm, (i.e., at the centreline and 100-mm height) is shown in Figure 2b. The distribution showed two distinct peaks. The first peak was for bubbles which had a mean diameter of 1.49 mm as mentioned above, whereas the second peak was the signal from the solid phase which had a typical value of 3 mm with an error range about 5%. As expected, the number of bubble signal was much more than that of solid particle in Figure 2b. The reason was that the measurement point was very near to the air source, so that the number of bubbles was expected to be much more than solid particles at this location.

Our previous work[19] investigated the two-phase (liquid-air) using the same bubble column with PDA measurements taken at three different air rates, namely 0.13, 0.25, and 0.38 L/min (corresponding to a gas fraction of 0.0065, 0.0138, and 0.0197, respectively). Comparing the liquid properties between the two-phase and three-phase investigations, the viscosities were nearly identical ($9.79 \times 10^{-4}$ Pa.s. for two-phase experiments, and $9.85 \times 10^{-4}$ Pa.s. for the three-phase experiments), but the densities ($1.002 \times 10^3$ kg/m$^3$ for the two-phase experiments, and $1.0485 \times 10^3$ kg/m$^3$ for the three-phase experiments) and surface tensions (0.0267 N/m for the two-phase experiments, and 0.0342 N/m for the three-phase experiments) were quite different.

It should be noted that the surface tension has an important effect on the bubble size. The surface forces on a bubble arise due to the linear surface tension acting on it, and they help a bubble to adhere to the edge of orifice delaying the detachment process.[22] Liow[23] reported that the surface tension forces in combination with the orifice diameter as well as thickness decide the bubble detachment time and hence the bubble size. Also, Hsu et al.[24] reported their observations about the mechanism in the presence of surfactants, where temporal variation of dynamic surface tension was taken into account. They pointed out the bubble size increased with surface tension even with the same sparger. The surface tension of the present fluid phase was higher than that in our earlier two-phase investigation, and as a result the bubble size was approximately 1.8 times larger.

### *Material properties*

The material properties of the liquid and solid phases used in this experiments are presented in Table 1. Deionized water was used as the liquid phase, with controlled amounts of soap and salt added to increase the surface tension and density. The water with added soap and salt can be regarded as a 0.15% Na(C18H35O2) and 7% NaCl solution. The viscosity was measured by a Brookfield Viscosity Liquid Bath (model K34710), and the surface tension was measured by Drop Shape Analysis System (model DSA100). The properties of the liquid were controlled for two objectives. First, the soap reduced the surface tension of the water, so that the bubbles were smaller and more rounded. Second, in the experiments, 3-mm acrylics polymethyl methacrylate beads were used as the solid phase, which had a density of$1.05\times10^3$kg/m$^3$ and, thus, slightly denser that water.

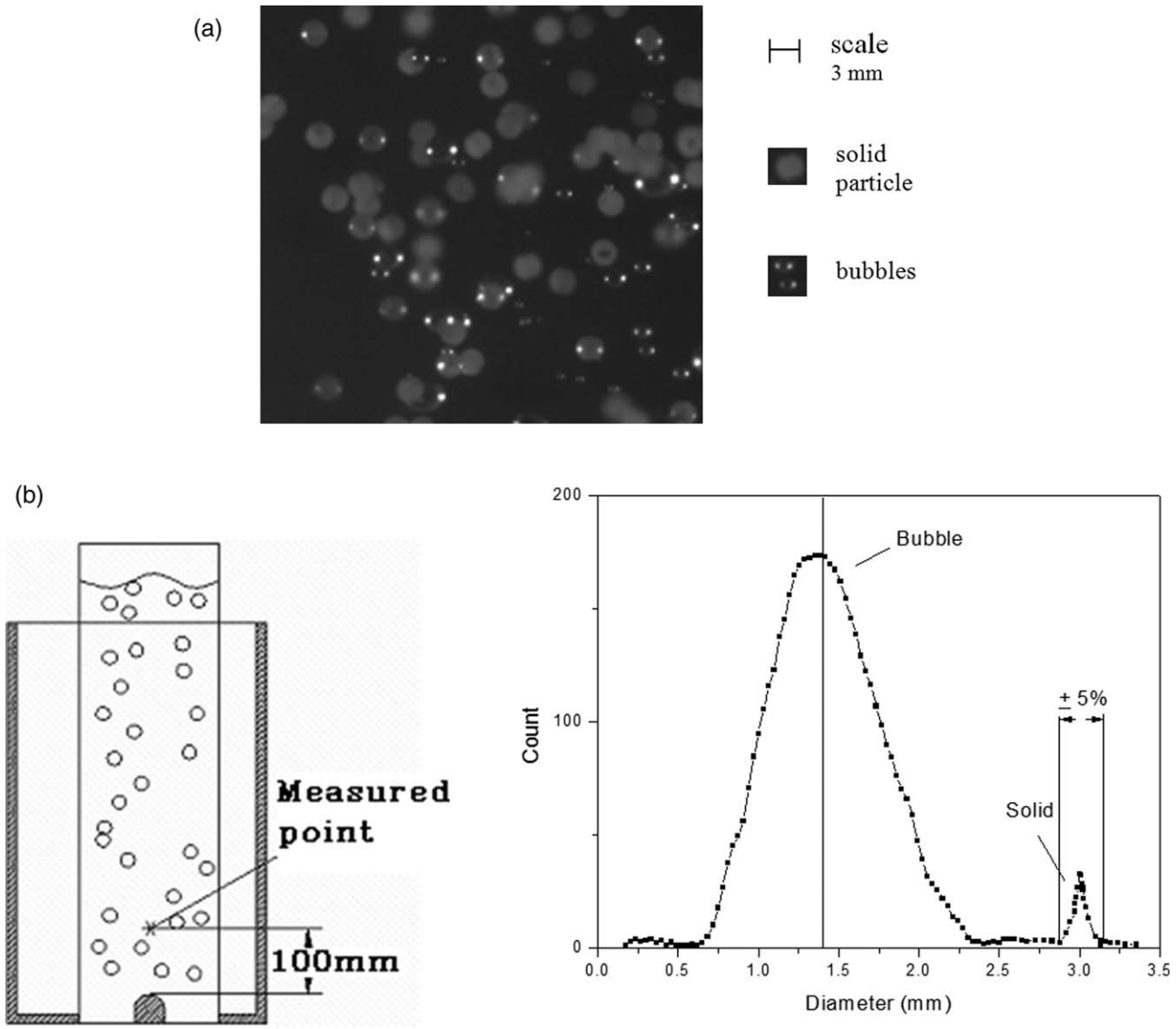


**Figure 2. (a) Photo of typical bubbles generated at an air flow rate of 0.4 L/min, (three-phase).**

**(b) Count distribution of all signal diameter at air flow rate of 0.4 L/min measured at $z = 100$ mm, $r = 0$ mm.**

Hence, salt was added so that the solution had a similar density with these beads. All tests were conducted at ambient pressure, and the liquid temperature was held constant to within $\pm 0.5$°C during the experiments.

### *PDA setup*

The fiber PDA setup with the principal components, that is, transmitting and receiving optical units, receiver module, and signal processor, is schematically shown in Figure 1. The experiments were divided into two parts for every measurement point. The first part was to measure the liquid velocity. The important parameters of PDA for measurements of liquid velocity are summarized in Table 2. To distinguish the liquid phase from the gas and solid phase, the liquid was seeded with hollow glass spheres as tracers (Type S-HGS DANTEC) at a concentration of 0.06 g/L in

**Table 1. Properties of the Liquid and Solid Phases**

| Liquid | Water with 0.15% Na(C18H35O2) and 7% NaCl |
|---|---|
| Liquid viscosity | $1.003 \times 10^{-3}$ Pa s |
| Liquid surface tension | 0.0342 N/m |
| Temperature | 20°C |
| Liquid density | $1.0485 \times 10^{3}$ kg/m$^3$ |
| Solid density | $1.05 \times 10^{3}$ kg/m$^3$ |

**Table 2. Optical Setting of Fiber PDA Measurement**

| Optical Setting | For Liquid Phase | For Bubble and Solid Phase |
|---|---|---|
| Wavelength of laser | 514.5 and 488 nm | 514.5 and 488 nm |
| Beams separation spacing | 38 mm | 15 mm |
| Beam half angle | 0.924° | 0.228° |
| Maximum measurement diameter | 412 $\mu$m | 3302 $\mu$m |
| Polarization of beam | Parallel | Parallel |
| Off-axis angle | 76° | 76° |
| Focus length of transmitting unit lens | 310 mm | 310 mm |
| Focus length of receiving unit lens | 500 mm | 500 mm |
| Number of maximum samples | 15,000 | 15,000 |
| Maximum elapsed time | 3000 s | 3000 s |

**Table 3. Air Flow Conditions for the Three Cases in the Three-Phase Experiment**

| | Air Flow Rate, $Q_G$ (L/min) | Superficial Gas Velocity, $V_G$ (mm/s) | Mean gas Volume Fraction, $\alpha$ |
|---|---|---|---|
| Case 1 | 0.4 | 0.376 | 0.0084 |
| Case 2 | 0.8 | 0.752 | 0.0168 |
| Case 3 | 1.2 | 1.128 | 0.0258 |

the water. The spheres had a mean size of 10 $\mu$m, a diameter range between 2 and 20 $\mu$m, and a material density of 1.4 g/cm$^3$. The tracers were small enough to following the flow in our test bubble column and because they were silver coated, the laser light can be reflected at their surfaces to generate strong scattering signals which can be received by the PDA detectors. As mentioned before, the bubbles had a size range from 600 to 2400 $\mu$m. The obvious difference between the size of the bubble and tracer limited all verified signals for this setup to be from the seeding particles. The second part was to measure both the size and velocity for the bubbles and solid particles. The important parameters of PDA for the second part are also shown in Table 2.

For both setup, the off-axis angle was an important prerequisite for the measurements of liquid and bubble velocities and bubble size. The scattering mechanism that was suitable for the PDA measurements of bubbly flow in this study was primarily reflection. Thus, the off-axis angle of 76° was chosen for both setups. Based on the consideration of Lorenz–Mie theory, the PDA receiving optics at 76° angle would receive the maximum signal from the dominating reflected light. The unused scattering lights, such as the first and second-order refraction lights, should be negligible.

A 3-D traverse system was used for the PDA to control the measurement positions. As shown in Figure 1, the glass wall facing the receiving optic was aligned in the direction normal to the axis of the receiver. This was to ensure that the normal lines of both transmitting and receiving unit lens were perpendicular to the rig surface. The effective focal length $f'$ for both lens were given by

$$f' = \frac{m_3}{m_1} f_0 + \frac{m_2 - m_3}{m_2} d + \frac{m_1 - m_3}{m_1} d_1 \quad (1)$$

Here, $f'$ is a function of $f_0$ (the focal length in air), $m_1$ (the refractive index for air), $m_2$ (the refractive index for the glass wall of the observation box), $m_3$ (the refractive index for water), $d$ (the thickness of the container glass wall), and $d_1$ (the distance between the lens and container wall).

The measurement planes are also shown schematically in Figure 1. The tip of the air stone was located at 50 mm above the bottom of the bubble column. The subsequent location for measurement ($z$) was referenced from the top of the air stone. Measurements at each location lasted at least 30 min, and the total number of validated samples obtained ranged from 5000 to 15,000. As far as the time-averaged behavior of the bubble column dynamics was concerned, the flow distribution could be considered symmetrical (note that the symmetry was also verified with spot measurements and flow visualization), and, thus, the measurements were taken only on an half-plane (at $z = 100$, 130, 160, 200, 400, and 600 mm) and at 10 locations along the $r$ direction(at $r = 0$, 10, 20, 30, 40, 50, 60, 65, 70 and 75 mm). Given that the diameter of the bubble column was 152 mm, the radial position at 75 mm was, thus, the nearest measurement location to the wall.

## Results and Discussion

### *Preliminary measurements*

As mentioned earlier, the flow visualization picture in Figure 2a illustrates that the bubble diameters were much smaller than the diameter of the solid particles. Bubble coalescence was, therefore, expected to be low, except at regions near the air stone where the bubbles were highly concentrated. Within the bubble size range of the present experiments, the inaccuracy in the PDA measurements was expected to be small, and it was confirmed by the fact that the measurement repeatability was excellent for all cases. Overall, the measurement errors for the velocity and diameter were estimated to be within 3 and 15%, respectively.

*Superficial Velocity of Bubbles.* The superficial gas velocity $V_G$ is defined as

$$V_G = Q_G / A_{col} \quad (2)$$

Here, $Q_G$ is the air flow rate and $A_{col}$ is the cross-sectional area of the bubble column. In our investigation, the air flow rate was set at 0.4 (Case 1), 0.8 (Case 2), and 1.2 (Case 3) L/min, corresponding to the superficial gas velocity $V_G$ of 0.376 (Case 1), 0.752 (Case 2), and 1.128 (Case 3) mm/s, respectively.

The mean gas volume fraction $\alpha$ was determined by measuring the increase in the liquid level when air was introduced to the column, that is

$$\alpha = (1 + H_0/\Delta H)^{-1} \quad (3)$$

where $H_0$ is the initial liquid level and $\Delta H$ is the increased liquid level due to the pumped air. Thus, the air flow rates also corresponded to the mean gas volume fractions of 0.0084 (Case 1), 0.0168 (Case 2), and 0.0258 (Case 3). Table 3 summarizes the relationship for the air flow rate,

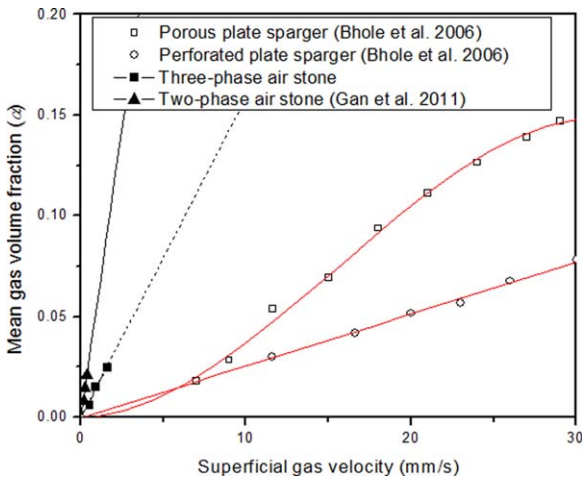


**Figure 3. Variation of average gas holdup with superficial gas velocity in the bubble column.**

**Profiles for porous and perforated plate sparger are reproduced from Bhole et al. (2006). [Color figure can be viewed in the online issue, which is available at wileyonlinelibrary.com.]**

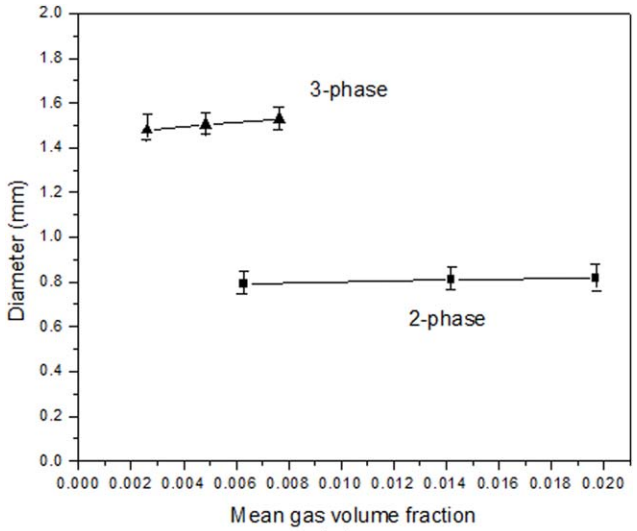


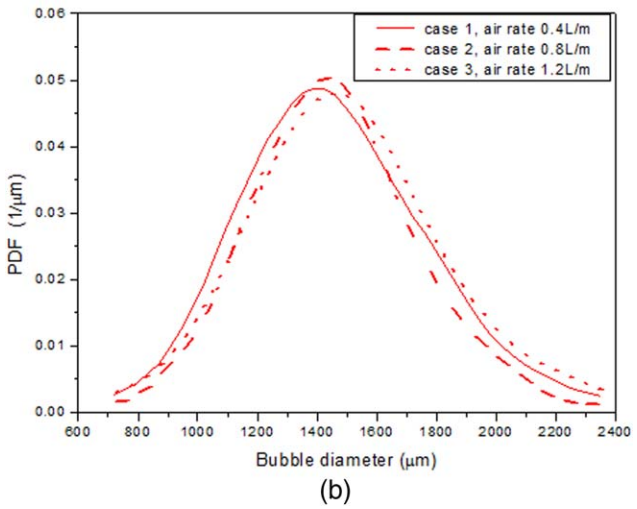


**Figure 4. (a) Mean bubble diameter as a function of mean gas fraction at $z = 600$ mm, $r = 0$ mm.**

**(b). Bubble-size distribution at $r/R = 0$ and $z = 600$ mm for the three cases in three-phase investigation. [Color figure can be viewed in the online issue, which is available at wileyonlinelibrary.com.]**

superficial gas velocity, and mean gas volume fraction for all three cases.

Joshi et al.[25] proposed the following function between the average gas holdup and superficial gas velocity for the homogeneous and heterogeneous regimes

$$\alpha \sim V_G^n \tag{4}$$

In Eq. 4, the value $n$ signifies the regime prevailing in the bubble column, with $n > 1$ corresponded to the homogeneous regime and $0.4 < n < 0.8$ to the heterogeneous regime. Figure 3 shows the variation of average gas holdup with the superficial gas velocity using the air stone in this study. The results of the two-phase investigation in Gan et al.[19] and two common types of spargers in a bubble column of similar geometry,[26] namely the porous and perforated plate spargers, are also shown. The relationship between the average gas holdup and superficial gas velocity for the air stone used in our two-phase and three-phase experiments was linear, that is, similar to that of the perforated plate sparger. In addition, $n$ was close to 1.0 suggesting that the flow field should be within the homogeneous regime. For the porous plate sparger, however, $n$ decreased with $V_G$ with a value at about 2 for $V_G < 10$ mm/s and smaller than 1 for $V_G > 15$ mm/s. This implies that, for the porous plate sparger in Figure 3, the flow field should be in either the transitional or heterogeneous regime. The profile gradient of the three-phase bubble column was smaller than that of the two-phase column but steeper than that of the perforated plate sparger. This suggests that the bubbles in the three-phase bubble column had a longer residence time than Bhole et al.[26] but shorter than the cases of two-phase investigation. In other words, for the same superficial gas velocity, the bubbles in the two-phase bubble column would spend twice the time to travel through the bubble column than the three-phase bubble column, and 20 times than the bubbles produced by the perforated plate sparger used by Bhole et al.[26] The reason should be due largely to the difference in bubble size. The bubbles had a bigger size (about 1.5-mm diameter) in our three-phase column compared to the two-phase bubble column (about 0.8-mm diameter) but smaller size than that of Bhole et al. (about 6-mm diameter). The smaller size bubbles had smaller terminal velocities and, therefore, were easier to be trapped in the large circulation cell. Hence, they travelled a longer journey inside the bubble column before reaching the top.

*Mean Bubble Diameter from Generator.* The mean diameters obtained from all measurement points at $z = 600$ mm for different mean gas volume fractions in both two-phase[19] and three-phase experiments are shown in Figure 4a. The mean bubble size was found to be approximately 1.5 mm, and it increased slightly with the mean gas volume fraction. In the three-phase experiments, it increased by about 5% with the air rate from 0.4 to 1.2 L/min. In contrast, the increase was only about 2% from 0.13 to 0.38 L/min. This might be due to the fact that bubble coalescence increased with the gas volume fraction due to two reasons. First, the air flow rate was larger in the three-phase experiments which enabled the bubbles to have more chances to merge with each other especially near the air stone. The second was due to the presence of the solid particles. With solid particles on the path of the rising bubbles, the bubbles would have more chances to collide when they were injected into the bubble column. Figure 4b shows that the bubble diameter distribution for the three cases of air flow rate. All profiles showed a normal distribution, and the bubble size standard deviation was about 10% for all the three cases.

*Mean Slip Velocity of Bubble at $r/R = 0$, $z = 600$ mm.* The mean difference between the bubble and liquid velocities and their slip velocity at the same point ($z = 600$ mm, $r = 0$ mm) as in Figure 4 for the three mean gas volume fractions are shown in Figure 5. In general, the mean slip velocity of bubbles decreased as the mean gas volume fraction increased. The slip velocity measurements can be fitted approximately by the following expression[27]

$$u_b = u_\infty (1-\alpha)^m \tag{5}$$

where $u_b$ is the bubble velocity, $u_\infty$ is the bubble terminal rise velocity, and $m$ is an empirical constant. Richardson and Zaki[27] suggested an approximated value of $m = 2.3$ for bubbles with Reynolds number ranged from 0.2 to 500. Ishii and Zuber[28] reported a value of $m = 2.0$ for bubbles with a Reynolds number near 250, whereas $m = 2.5$ was suggested

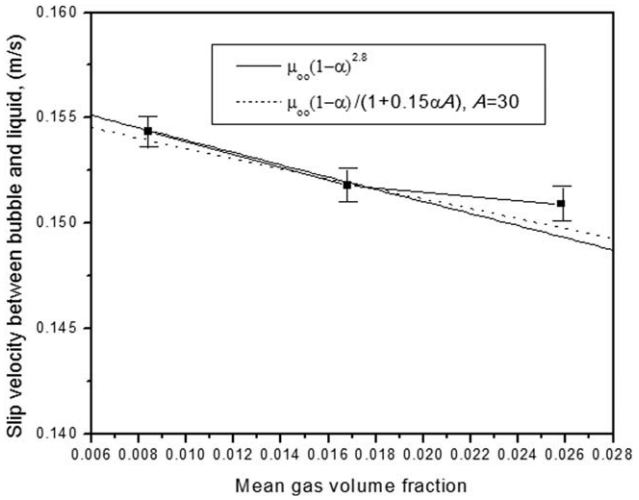


**Figure 5. Slip velocity between bubbles and liquid as a function of mean gas fraction at $r/R = 0$, $z = 600$ mm.**

**Here, $u_b$ is the bubble velocity, $u_\infty$ is the bubble terminal rise velocity $A = u_b^2/T_b$, and $T_b$ is the bubble velocity variance.**

by Zenit et al.[29] with the gas volume fraction from 0 to 0.2. From our present study, $u_\infty$ was found to be 0.169 m/s while $m$ was about 2.5, which agreed well with Zenit et al.[29] It should be noted that for the two-phase experiments, $m$ had a value of 2.8 which was larger than previously reported due largely to the effect of lower surface tension.

For a more precise determination for the velocity profile with a given mean gas volume fraction, Spelt and Sangani[30] derived the drag force on a homogeneous suspension of spherical bubbles rising through a fluid, and suggested that the mean bubble slip velocity $u_b$ can be expressed as

$$u_b = u_\infty \frac{(1-\alpha)}{1+\frac{3}{20}\alpha A} \tag{6}$$

where $A = u_b^2/T_b$, and $T_b$ is the bubble velocity variance. $A$ represents the stability of the bubble velocity, with a larger value corresponding to a more stable velocity.

Figure 6 shows that the mean value of $1/A$ in our three-phase experiments increased from 0.020 to 0.032, which corresponded to the value of $A$ from 50 to 31. Zenit et al.[29] presented a detailed discussion of the influence of mean gas volume fraction on the magnitude of $A$. Their experimental analysis resulted in a fitted function $A(\alpha)$ that decreased from 50 (at lower gas volume fractions) to about 10 (at a higher gas volume fraction of about 0.18). In this study, the three gas volume fractions were located on the part of low gas volume fraction in Zenit et al.,[29] which implied that our $A$ value agreed well with their analysis because they suggested the $A$ value should be within the range from 30 to 50 for $\alpha < 0.04$. The normalized variance, which is the inverse of $A$, increased with the mean gas volume fraction and had a value of about 0.03 for the three cases. It should be noted that the increased air flow rate would promote bubble–bubble hydrodynamic interactions, which in turn increased the bubble velocity variance and decreased the mean bubble velocity correspondingly.

However, it should be noted that the value of $A$ had a smaller value at about 10 for the two-phase experiments in Gan et al.[19] This means that the bubble velocities for the three-phase experiments were more stable than the two-phase experiments. The normalized variances of the solid particle velocity for all three cases are also added in Figure 6. It is clear that the solid velocity had a much bigger $A$ value, and the trend of $A$ for the three-phase bubble velocity was similar to that of the solid particles. According to the no-slip condition, the liquid velocities must have a zero slip velocity to the solid surface, and the bubble velocity variance will decrease due to the viscous dissipation as the solids travel with the bubbly flow. Because $A$ represents the stability of the velocity, it is, thus, reasonable to speculate the solid particles provide additional stability to the bubble velocity.

### *Measurements of the entire flow field*

The net liquid flow across a cross-section should be zero inside a bubble column due to continuity, and the same should be true for the solid phase. In addition, the liquid and solid phases should follow the bubbles moving upward around the column center and returned along the wall. Large-scale circulations are typical in bubble columns.[31] However, they may not be steady. For example, Chen et al.[32] observed that the flow field in the bubble column was formed by a meandering central bubble plume accompanied by smaller vortical structures near the wall. The same was also reported in our earlier two-phase experiments.[19]

In the early part of this study, preliminary visualization tests were conducted, and the flow behavior in the model bubble column exhibited clearly large-scale symmetrical circulations as shown schematically in Figure 7a. An instantaneous picture at the air flow rate of 0.8 L/min from $z = 100$ to 300 mm is also shown in Figure 7b. The injected bubbles swarm rose from the generator forming a bubble plume in the center and then subsequently dispersed in the upper part of column. On either side of the bubble plume, the liquid moved downward forming vortices with lower bubble concentrations. Beyond this region, the bubbly flow became relatively uniform across the cross-section, and the bubbles had a near homogeneous distribution. Figures 8, 9, and 10 show the profiles of the time-averaged mean axial bubble velocity and size, liquid and solid velocities, and volume fraction

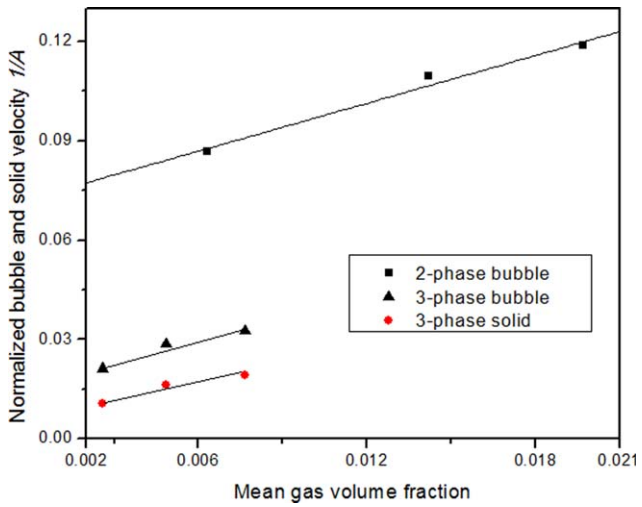


**Figure 6. Normalized bubble and solid velocity variance $T_b/u_b^2$ as a function of mean gas fraction for both the two-phase and three-phase bubble column at $r/R = 0$, $z = 600$ mm.**

**[Color figure can be viewed in the online issue, which is available at wileyonlinelibrary.com.]**

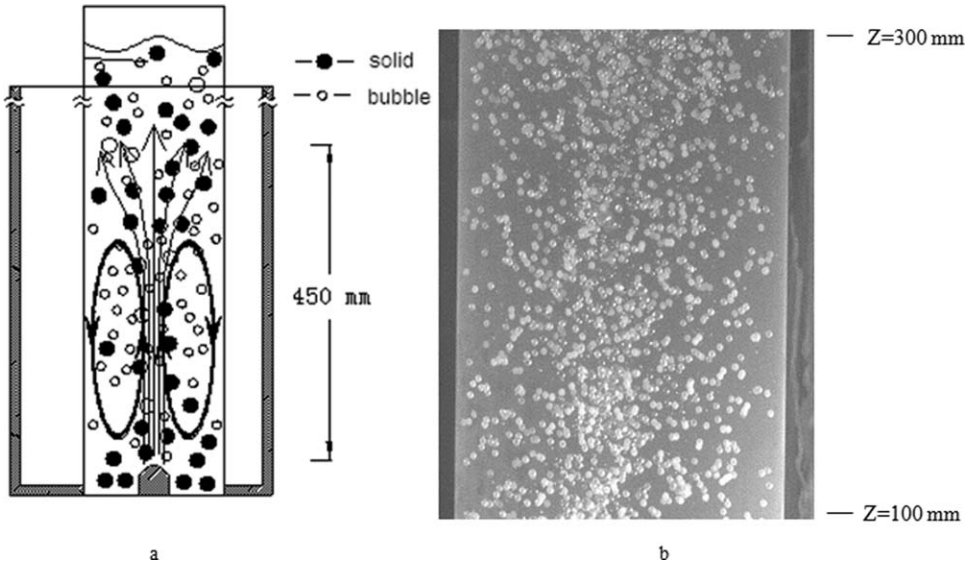


**Figure 7. (a) Sketch of flow field observed in the bubble column, (b) a snapshot of bubble column with the air rate of 0.8 L/min from $z = 100$–300 mm.**

distribution for the three phases at six consecutive $z$ locations with the air flow rate of 1.2 L/m.

Time-*Averaged Bubble Distribution in Bubble Column (Bubble Velocity and Size).* The left hand side of Figure 8 shows the spatial distribution of the mean bubble velocity. Similar to that of the two-phase experiments, the bubbles velocity development from $z = 40$ to 100 mm had a general increasing trend away from the generator. In contrast, the bubbles showed very low and occasionally negative velocities near the wall. The reason may be due to the fact that it was harder for the larger size bubbles (with higher buoyancy forces) to diffuse to the wall region, whereas the smaller bubbles can better disperse toward the wall region and move together with the returned liquid flow near to the wall. Comparing with the bubble velocity profiles of the two-phase experiments,[19] the bubble velocities were obviously higher in this study due to the relatively larger bubble sizes, as expected.

From $z = 400$ to 600 mm, the bubble velocity profiles showed that the bubble column had reached the quasisteady development stage with very little change between the two $z$ locations. The bubble diameters were relatively larger at the center of the column. Thus, the bubbles had a higher rise velocity due to larger buoyant forces and with near vertical rising trajectories, and they induced the liquid and solid to move up along the center region. The bubbles near the wall were slowed down by the drag of the downward moving liquid. The bubbly flow with the present air stone showed a higher velocity for bubble phases at lower heights close to the centerline for all cases. The velocities near $z = 100$ mm and $r/R = 0$ were larger than the terminal velocities of the

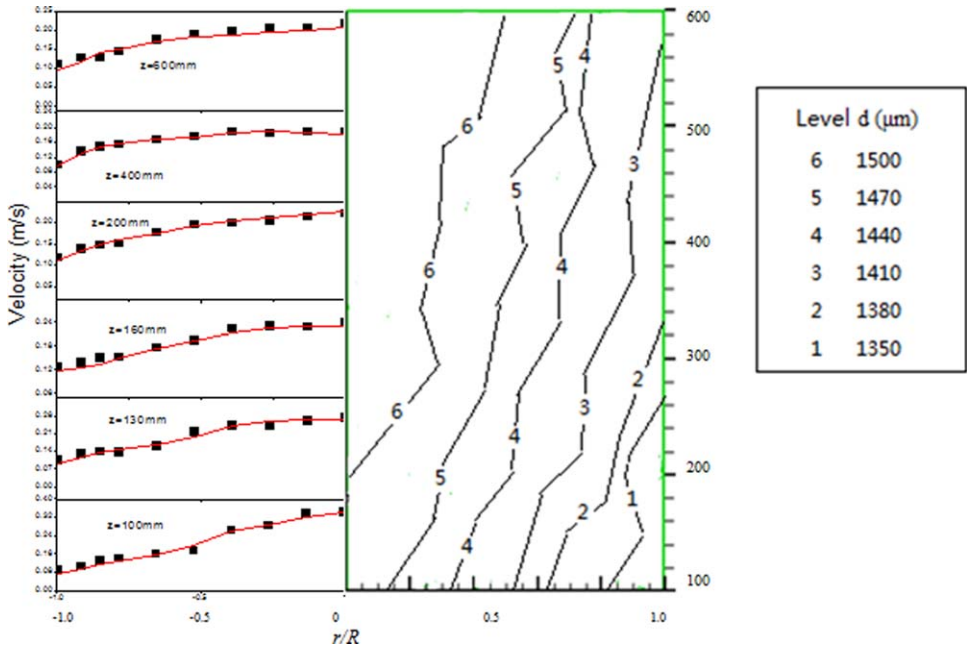


**Figure 8. Profiles of bubble time-averaged velocity and contours of the mean bubble diameter at the air flow rate of 1.2 L/min.**

**[Color figure can be viewed in the online issue, which is available at wileyonlinelibrary.com.]**

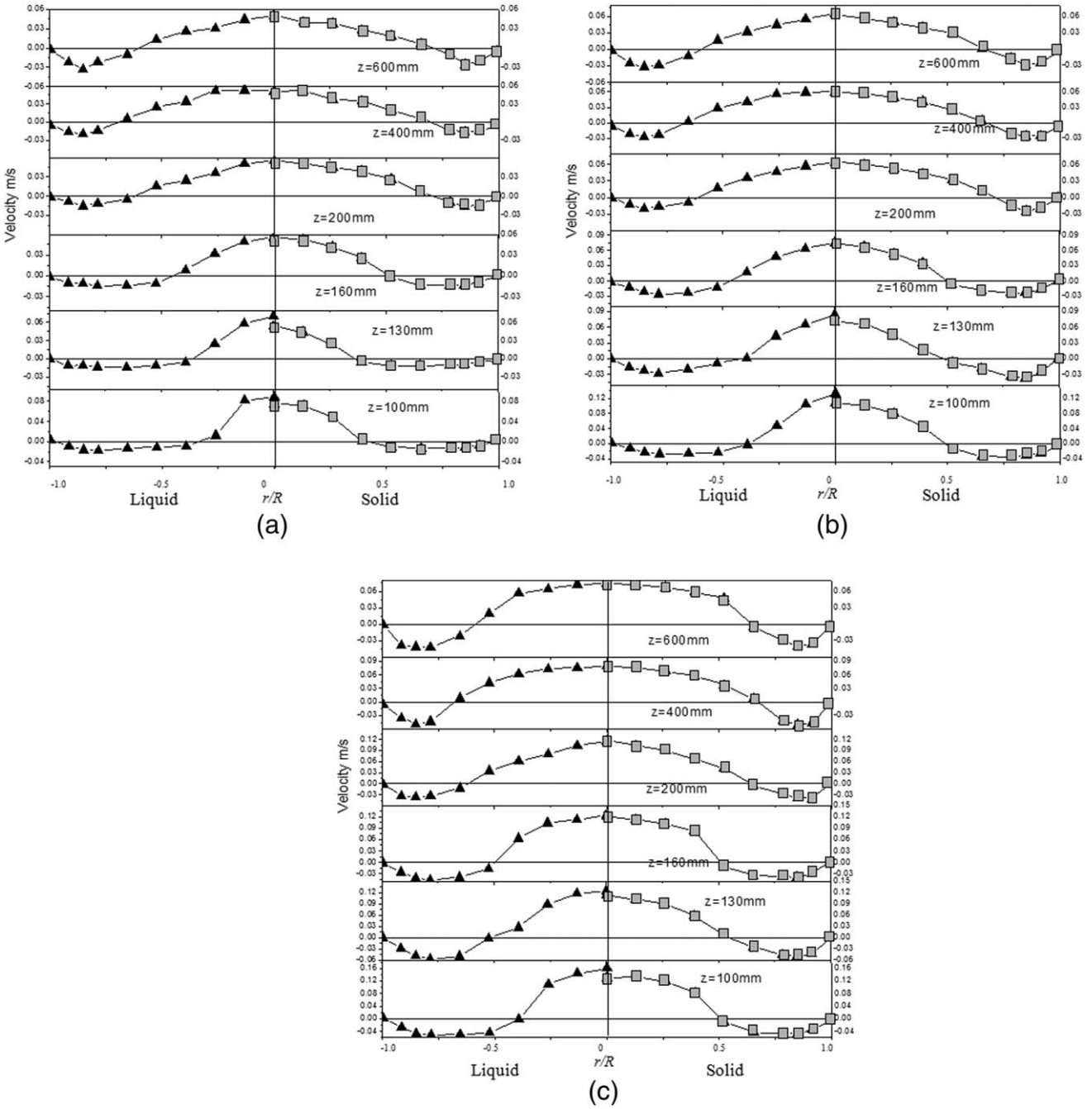


**Figure 9. (a) Profiles of the liquid and solid-phase time-averaged velocity at air flow rate 0.4 L/min.**

**(b) Profiles of the liquid and solid-phase time-averaged velocity at air flow rate 0.8 L/min. (c). Profiles of liquid and solid-phase time-averaged velocity at the air flow rate of 1.2 L/min.**

average size bubbles. Near the bubble generator, the swarm effect became significant. Meanwhile, the wall region at lower heights on either side of the bubble generator had lower liquid velocities, implying the presence of a relatively placid field with lower shear forces in the bubble column (also shown in Figure 7). Generally, the trend of the bubble velocity profile was similar to that of the two-phase investigation. Hence, the presence of the solid phase had insignificant influence to the time-average distribution of the bubble velocities at low-solid volume fractions (in our cases, no more than 0.5%).

The bubble-size distribution is an important representation of the hydrodynamic behavior in the three-phase bubble column. The right-hand side (RHS) of Figure 8 shows the mean bubble diameter contours at the air flow rate of 1.2 L/min. As mentioned before, the coalescence of bubbles was not significant due to the low air and solid fractions except near the air stone. It was clear that the signals from the local bubble size measurements were very scarce at the corner of the column for the three cases, and the signals only showed very small bubble diameter in these position. The bubble diameter contours also showed good agreement with the presence of the large-scale circulation. The larger bubbles were concentrated at the centerline and ascended to the upper of the bubble column, meanwhile the smaller bubbles were travelled with the downward flow to the corner of the bubble

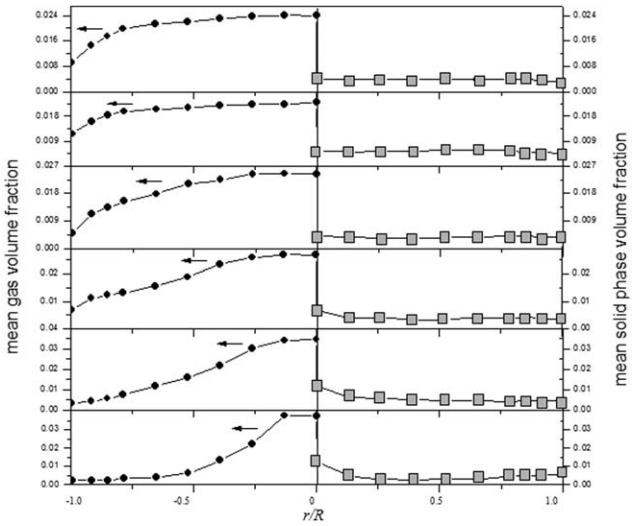


**Figure 10. Profiles of gas and solid-phase volume fraction at the air flow rate of 1.2 L/min.**

column. The bubble diameter contours shown that the bubble column was filled with this larger-scale circulation. It was, thus, clearly different from the two-phase experiments,[19] which besides the large-scale circulation there were small corner vortices formed by the shear between the downward flow of large-scale circulation and the wall. This might be attributed to the higher air flow rates for the three-phase experiments, and hence the bubbles were more energized and were not trapped at the corner.

*Time-Average Velocity of Liquid and Solids.* As shown in Figure 9, the liquid velocity, which was mainly induced by the drag force of the bubbles, reached its maximum at about $z = 100$mm for all the three cases. Beyond this height, the liquid velocity near the centerline decreased due to the entrainment of the slower moving liquid from the surrounding, and also the reduction in the air volume fraction. This corresponded to a decrease in the bubble density and, as a consequence, the drag force on the liquid phase exerted by bubbles was also reduced. Overall, the liquid velocity profile in this study was similar to the two-phase experiment.

The fundamental mechanisms for particle entrainment and de-entrainment in a three-phase fluidize bed had been studied by Bavarian and Fan.[33] Particle entrainment normally decreases with a decrease in bubble size and bubble frequency, and with an increase in liquid velocity and particle size. Lau et al.[34] indicated that the liquid entrainment rate increases with the system pressures and gas velocities. The same behavior occurred in this three-phase study. When the air rate increased which implied a higher bubble frequency, the velocities of both the solid and liquid circulation increased as shown in Figure 9. The velocity profiles also showed that the magnitude of the liquid and solid circulation generally increased with the mean gas volume fraction. The balance position at which the mean liquid and solid particle axial velocity equaled to zero shifted toward the wall with increasing $z$, implying that the bubble plume gradually extended to the entire cross-section of the bubble column. For a short distance above the air stone, the width of the bubble plume became narrower but with a higher gas volume fraction. As the bubble plume increased its width by entrainment at higher level, the amount of liquid and solid phases being entrained upward also increased correspondingly, and the velocities of liquid and solid phase decreased. It should be noted that the integral over the mean liquid velocity profiles yields values close to zero for all three cases, when the radial profiles of the gas volume fraction are taken into account. A detailed calculation can give the errors between these integrals of upward and downward flow over the column cross-section was no more than 5%, which is similar to the value of error reported by Mudde and Saito.[35]

*Time-Average Volume Fraction Flow Distribution.* Figure 10 shows the distribution of the bubble and solid-phase volume fraction. The time-average gas volume fraction was deduced from the PDA measurements using the following equation[18]

$$c_{\mathrm{v,g}} = \frac{\pi}{6}\frac{1}{\Delta t}\sum_{i=1}^{N}\frac{d_{\mathrm{b},j}}{|\vec{U}_{\mathrm{b},i}|}\frac{1}{A_{\mathrm{pv},i}} \tag{7}$$

where $A_{pv,i}$ is the effective probe volume cross-section of the PDA system from which scattered light signals are detected, $d_{\mathrm{b},i}$ is the diameter of the measured bubble, $\vec{U}_{\mathrm{b},i}$ is the measured velocity of signal, $N$ is the number of samples, and $\Delta t$ is the measured time. The value of $A_{pv,i}$ depends on the bubble size and on the area of $150 \times 150\,\mu\mathrm{m}^2$of the illuminated probe volume

$$c_{\mathrm{v,s}} = \frac{\pi}{6}\frac{1}{\Delta t}\sum_{i=1}^{N}\frac{d_{\mathrm{s},j}}{|\vec{U}_{\mathrm{s},i}|}\frac{1}{A_{pv,i}} \tag{8}$$

Equation 8 is used for the calculation of the volume fraction for the solid phase. The only difference between the two equations is that the $d_{\mathrm{s},j}$ has a fixed value of 3 mm in Eq. 8.

The mean air volume fraction in each of the profile was found to be lower than that determined by the change of liquid level when the gas was injected. This was due to the bubbles and solid particles blocking part of the signals received by the PDA, and the number of missed signals increased with the air volume fraction. In our investigation, the maximum error was estimated to be about 12.7% for Case 3 with the air rate of 1.2 L/min. Table 4 shows all the errors for three cases. The same level of accuracy was also reported by Brenn et al.[18] It is reasonable to estimate that there was a similar magnitude of accuracy for the volume fraction of the solid phase.

For all the three cases, the bottom corners had smaller gas volume fractions than at the other regions. This can be explained by means of the large-scale circulation. The bigger bubbles moved upward along the column quickly. The liquid circulation can only entrained the smaller bubbles to move into the core of the circulation cells. Another trend, as shown

**Table 4. Estimated Errors for the PDA Measured air Volume Fraction**

| | Air Volume Fraction (calculated by the Difference of Liquid Level), $\alpha$ | Air Volume Fraction (measured by PDA), $\alpha_1$ | Measurement Error of Air Fraction $(\alpha - \alpha_1) \times 100\%$ |
|---|---|---|---|
| Case 1 | 0.0084 | 0.0079 | 5.9% |
| Case 2 | 0.0168 | 0.0152 | 9.5% |
| Case 3 | 0.0258 | 0.0225 | 12.7% |

by the arrows marked in the RHS of Figure 10, was that the maximum local air volume fraction tended to move toward the column wall with increasing heights. This phenomenon is known to be a typical bubble coherent behavior for low superficial velocities[36] caused by the complex interactions of multiple phases including the drag and lift forces.[37]

The profiles of solid-phase volume fraction showed nearly uniform distribution, except for some peaks near the generator due to stronger bubbly motion. The average solid-phase volume fraction decreased with the height $z$, which was due to the heavy density of the solid. Not all the solid particles can reach the top of the bubble column.

Both the gas and solid-phase volume fractions increased with the superficial gas velocity. The gas volume fraction profiles behaved similar to the two-phase experiments. At the lower part of the column, the solid-phase volume fraction increased in a linear relation with the air flow rate. However, at the upper part of the column, the solid-phase volume fraction for 1.2 L/min was almost 8.7 times that of 0.4 L/min. It indicated that the solid particles needed higher momentum from the liquid phase to move along the column.

*Slip Velocity*. The slip velocities between the liquid and other two-phases for the air flow rate of 1.2 L/min are shown in Figure 11. It is clear that the slip velocities with bubbles were larger than that with solid at all points. Another fact is that the absolute values of the slip velocities between liquid and solids were no more than 20% of the absolute values of the liquid velocities except the region near the wall. For the wall region, both of the liquid and solids velocities were very small. This indicates that the solid phase can follow closely the movement of the liquid phase. At lower positions ($z < 400$ mm), the slip velocities with bubbles were smaller except at several points near the center which might be due to the smaller size bubbles distribution near the wall (as shown in Figure 8). Correspondingly, higher slip velocities were observed in regions with higher bubble concentrations.

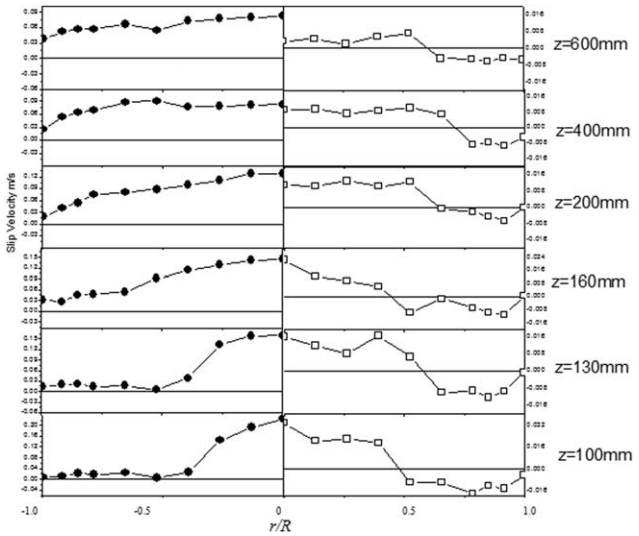


**Figure 11. Profiles of the high and low mean axial slip velocities for the air flow rate of 1.2 L/min (LHS: slip velocity for bubbles with liquid, RHS: slip velocity for solid phase with liquid).**

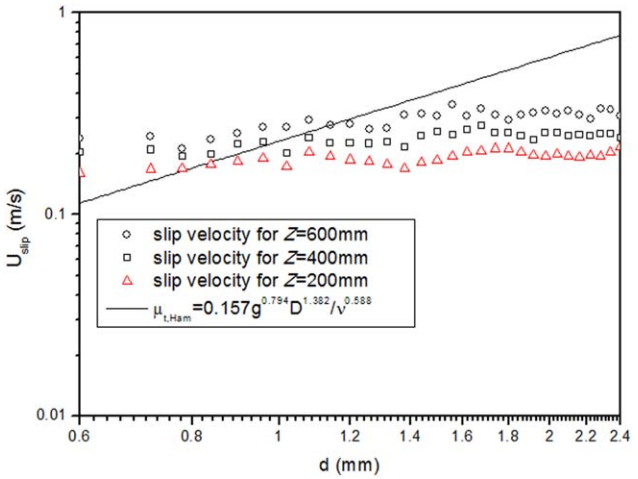


**Figure 12. Slip velocity between bubbles and liquid as a function of the number mean bubble size at $z = 600$ mm for air rate 0.8 L/m (Case 2).**

**[Color figure can be viewed in the online issue, which is available at wileyonlinelibrary.com.]**

The slip velocities between the solid and liquid decreased with the height. The solid particles obtained the initial momentum from the liquid near the bottom of the bubble column. At points just above the bubble generator, the slip velocities for the solid phase were slightly higher than that at other locations. This phenomenon can be attributed to the jet effect of the bubble swarm as shown earlier in Figure 7. The high bubble concentrations would entrain the neighboring solid to follow the bubble swarm and move faster than liquid. As the bubbles and solid particles dispersed at higher $z$, the slip velocity between solid and liquid phase decreased correspondingly due to the dispersion of the energy of bubbles and solid particles.

Figure 12 shows the bubble slip velocities against the mean bubble diameter for all the measurement points at $z = 600$ mm for Case 2. A function for the terminal velocities of single bubble for $4 < Re < 100$ was proposed by Hamielec et al.[38] as

$$u_{t,\mathrm{Ham}} = 0.157 \frac{g^{0.794}}{\nu^{0.588}} D^{1.382} \tag{9}$$

The function is also plotted in the figure for comparison.

In general, the slip velocity increased with the bubble size, because larger bubble had a higher terminal velocity, but the increase was not as steep as the increase of terminal velocity. It is known that larger and faster bubbles drives the flow and draws up smaller bubbles via hydrodynamic interactions between the bubbles and the turbulence.[4] The data in Figure 12 show that the measured slip velocities of the smaller bubbles exceeded the theoretically predicted terminal velocity of a single bubble with the same size, but the slip velocities of larger bubbles were all below the terminal velocities. The larger bubbles lost their momentum by the drag force from the liquid, and the smaller bubbles were accelerated by larger bubbles. The critical size appeared to be about 1200 $\mu$m.

Figure 13 shows the drag coefficients of the bubbles against the Reynolds number for the three cases. The

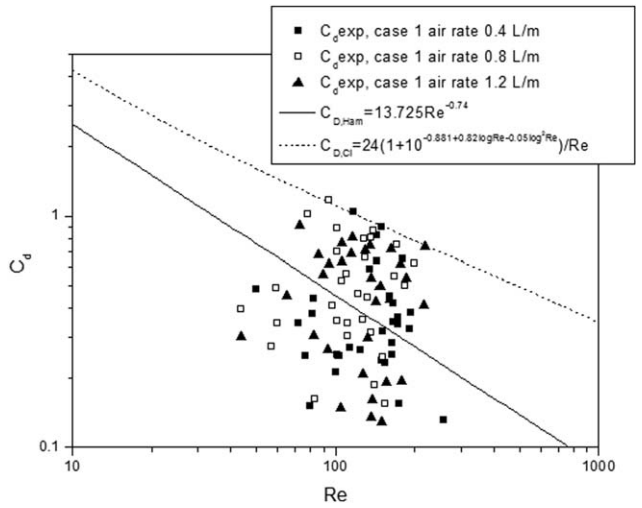


**Figure 13. Drag coefficient of the bubbles as a function of Reynolds number formed with the slip velocity for all three cases.**

analytical function for single bubble shown in this figure is proposed by Hamielec et al.,[38] that is

$$C_{D,\mathrm{Ham}} = 13.725\mathrm{Re}^{-0.74} \tag{10}$$

which is valid for fluid sphere. Clift et al.[39] also suggested another relationship for the drag coefficients of solid particles in liquid

$$\log_{10}\left(\frac{C_{\mathrm{D.Cl}}\,\mathrm{Re}}{24}-1\right) = -0.881+0.82\log_{10}\mathrm{Re}-0.05(\log_{10}\mathrm{Re})^2 \tag{11}$$

The present results show that the trend of drag coefficients for bubbles in the three-phase experiments matched the behavior of fluid spheres. For solid particles, due to the low Re (<1), the correlation of drag force given by Tomiyama[40] can be used as follow

$$C_{\mathrm{D}} = \frac{8}{3}\frac{Eo}{Eo+4} \tag{12}$$

where $Eo = \frac{g(\rho_l-\rho_g)d_s^2}{\sigma}$.

For the solid particle, $g$, $\rho_l$, $\rho_g$, $d_s$ and $\sigma$ were all constant, and the constant drag coefficient of $C_{\mathrm{D,s}} = 2.63$ can be calculated. Figure 13 shows that for most bubbles, the drag coefficient was smaller than that of solid phase.

*Stability from Solid Phase.* As mentioned before, there are two principal flow regimes in bubble column reactors: homogeneous and heterogeneous.[41–43] In the homogeneous regime, the bubbles rise roughly vertically with small vertical and horizontal fluctuations. Bubble coalescence and break-up are negligible, and no large-scale liquid circulations occur near the bed. The long-time-average radial profiles of gas volume fraction and liquid velocity are mostly flat. In the heterogeneous regime, on the other hand, the bubble-size distribution is wide, and bubble coalescence is promoted and macroscale circulations of the liquid phase are present. The long-time-average radial profiles are roughly parabolic with a maximum at the center.

In our previous two-phase experiments,[19] the heterogeneous regime was formed due to bubble plumes meandered within the column, a behaviour that had also been observed by Brenn et al.,[18] Kulkarni et al.,[44] and Warsito and Fan.[11] The meandering bubble plumes caused fluctuations in the flow velocity measured by the PDA at a single point, which was obviously different from the high-frequency fluctuations caused by consecutive bubbles passing through the measurement volume of the PDA. A two Gaussian distribution model can, thus, be used to depict the velocity distribution for a single point in this kind of heterogeneous regime. Figure 14a shows an example of the fluid velocity distribution in the two-phase experiments.[19] However, there is no such two Gaussian distribution model in this three-phase study. This suggests that the solid phase stabilizes the flow field of the bubble column. A typical example of the fluid velocity distribution in this three-phase study is shown in Figure 14b.

The detailed flow visualization shown in Figure 15 illustrates the change of bubble plume behavior with the solid-phase volume fraction. Figures 15a, b show that the bubble plume meanders in the column without the solid phase within the $z$ range from 65 to 340 mm for Case 2 with the

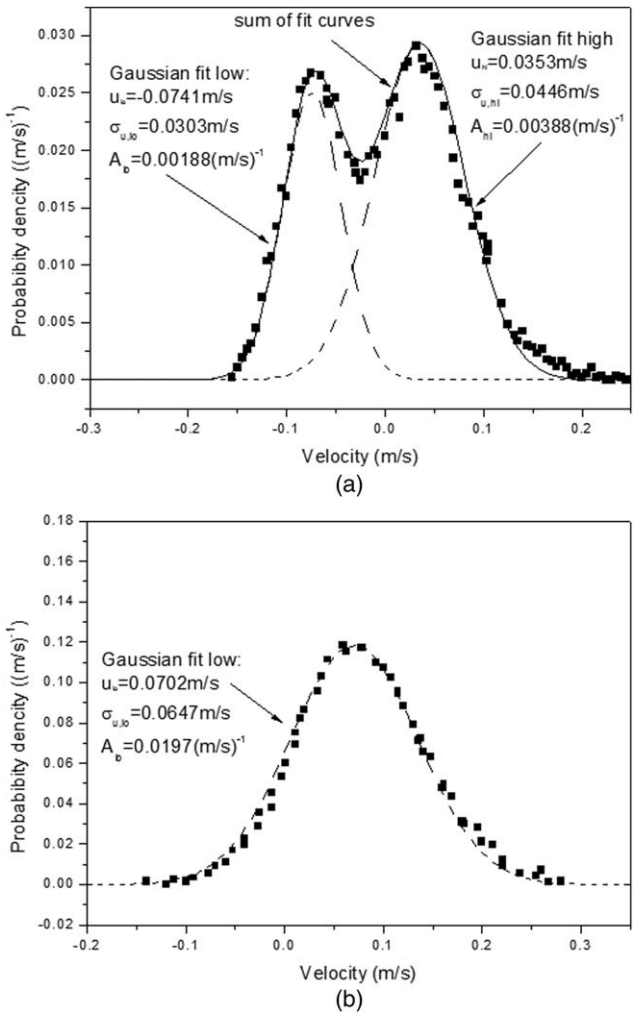


**Figure 14. (a) Liquid velocity probability density distribution (pdf) by the superposition of two Gaussian functions at $z = 400$mm and $r = 60$ mm at the air flow rate of 0.25 L/min for the two-phase experiments.**

**(b) Liquid velocity probability density distribution (pdf) by the superposition of two Gaussian functions at $z = 400$ mm and $r = 60$ mm at the air flow rate of 1.2 L/min for the three-phase experiments.**

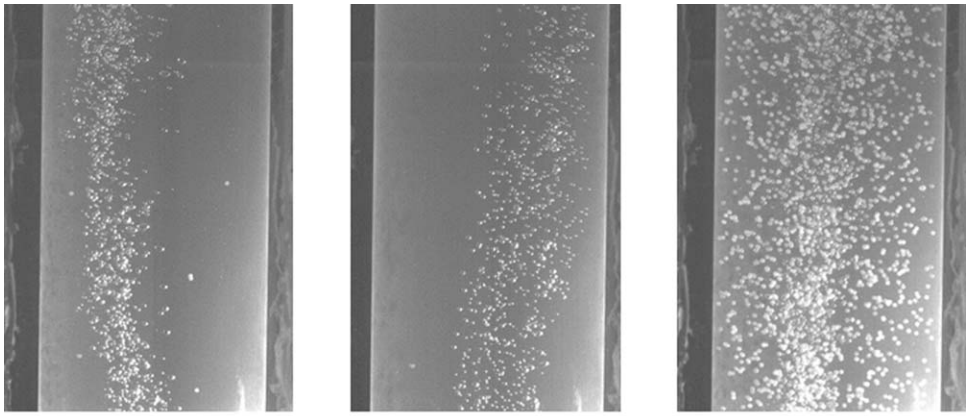

a. without solid phase b. without solid phase c. three-phase bubble column

**Figure 15. Bubble plume behaviors for Case 2, height from $z = 65$–340 mm.**

air flow rate of 0.8 L/min, and the bubble plume behavior for the three-phase bubble column is shown in Figure 15c. Without the solid phase, the bubble plume cannot rise up along the centerline steadily, and sway from side to side. In our earlier two-phase experiments, it had a swaying frequency of about 0.036 Hz.[19] In this three-phase investigation, as shown in Figure 15c, the bubble column clearly just moved up along the centerline steadily.

Mena et al.[45] reported similar observation in a 140-mm diameter bubble column, and concluded that for a solid-phase volume fraction under 3%, the increased solid-phase would stabilize the flow field. In our investigation, the maximum solid-phase volume fraction was 1.2%. By increasing the solid-phase volume fraction in steps, that is, 0.24% each time, the lowest solid-phase volume fractions to stabilize the bubble plume can be determined. The lowest solid-phase volume fractions to stabilize the flow field for the three cases are shown in Table 5.

### *Stability criterion based on the influence of lift force*

The flow patterns in the bubble column had exhibited different behavior between the two-phase and three-phase. It was typically homogeneous for the above three-phase experiments, whereas it was heterogeneous in our earlier two-phase experiments. For industrial reactor design and operation, it is important to know the range of parameters which respective regime prevails. This naturally leads to the stability issue as well as the regime transition condition. Ruzicka and Thomas[46] used the Rayleigh–Benard instability in thermal convection to explain the transition between the homogeneous and heterogeneous regimes. Based on their theory, the column dimensions, effective viscosity of bubbly mixture, and hydrodynamic diffusivity of bubbles are all used to explain the flow transition. In this study, we consider the additional effect of the presence of the solid phase, which has not been explicitly included in the aforementioned theory.

**Table 5. The Lowest Solid-Phase Volume Fraction (0.24% per Step) for Stabilizing the Bubble Plume**

| Air Flow Rate (L/min) | 0.4 | 0.8 | 1.2 |
|---|---|---|---|
| Minimum solid-phase volume fraction of stabilization | 0.24% | 0.72% | 0.96% |

In our earlier two-phase studies,[19] bubble swarm would sway in the column from side to side with a frequency about 0.036 Hz. Similar behavior was also observed in the experiments by Brenn et al.[18] and Warsito and Fan.[11] Some researchers used the influence of the lift force generated by the rotation of the liquid flow field combining with the slip velocity between bubble and the surrounding liquid to explain this phenomenon[47,48]. Lucas et al.[49] investigated further the role of the bubble lift force on the stability of a two-phase bubble column by applying the automatic control theory. Their criterion for stability with lift force agrees well with our experimental investigation of the two-phase bubble column.[19] For the analysis of the stability of the flow filed in our three-phase bubble column, the automatic control theory may also be applied to our homogeneous three-phase flow model. In this model, an initial perturbation, that is, a local increase of the gas volume fraction, is applied on a small region of the flow field, the vertical liquid velocity will then increase with the gas volume fraction. Due to the lift force, the large bubbles migrate into this region and increase the gas volume fraction again. This is considered as a positive feedback for an initial disturbance of the local gas volume fraction in the bubble flow.[49] For the stability of a three-phase bubbly flow, the influence from the solids is unclear as to whether it is able to compensate this positive feedback of the bubble lift forces. To answer this question, an analysis of stability in a three-phase homogenous flow with monosized bubbles and solid particle will be performed below. An approximated criterion for an estimation for a given continuous bubble-size distribution in a three-phase bubble column is proposed. The proposed criterion will be compared with our experimental results.

*The Three-Phase Flow Field Model.* The following analysis focuses on the stability of a 2-D flow pattern in a three-phase bubble column. The model excludes the effect of the wall and the bubble generator (i.e., it does not consider the wall region and the sparger region).

For a small region in the undisturbed homogeneous flow regime with monosized bubble size in a three-phase bubble column shown in Figure 16a, the liquid is used as the reference which means that the liquid superficial velocity is assumed to be zero. The bubbles rise with a constant

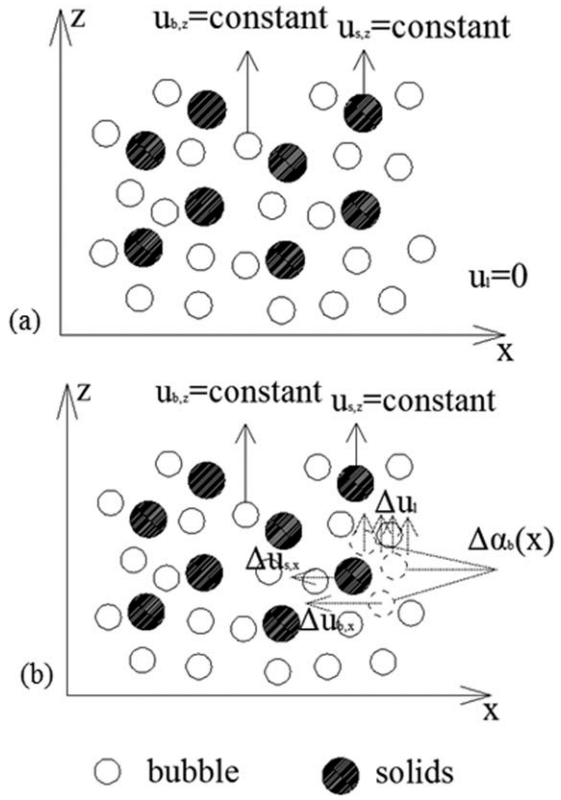


**Figure 16. (a) A simplified 2-D model for a small region in the undisturbed three-phase homogeneous flow field.**

**(b) A simplified 2-D model for a small region in the three-phase homogeneous flow field with a perturbation $\Delta\alpha_b(x)$.**

velocity in $z$ direction which only depends on the bubble diameter and the liquid properties. For the solid particles, the velocity is constant in the $z$ direction too. In the homogeneous flow field, the time-averaged holdup and velocity is steady for both bubbles and solids. The homogeneous flow field is undisturbed. The following relations may be used

for liquid phase, $\vec{u}_l(x,y,z,t)=0$, =
for bubble phase, $\vec{u}_b(x,y,z,t)=u^0_{b,z}\vec{e}_z$ and $\alpha_b(x,y,z,t)=\alpha^0_b$,
for solid phase, $\vec{u}_s(x,y,z,t)=u^0_{s,z}\vec{e}_z$ and $\alpha_s(x,y,z,t)=\alpha^0_s$

To describe the disturbed three-phase homogeneous flow field with a local increase of the gas volume fraction $\Delta\alpha_b(x)$, the following approximations and assumptions for the bubble and liquid phase for the two-phase bubbly flow, are used to establish the set of partial differential equations in this analysis[49]

1. The liquid velocity (ul) has only a component in the vertical direction due to the disturbances. =
2. The gradients of the liquid velocity occur only in × direction.
3. The only driving force for a change of the vertical liquid velocity is assumed to be a local change of the averaged density.
4. Beside the constant vertical velocity of the bubble phase (ub,z), a component of the bubble velocity (ub,x) may occur in (horizontal) x direction for the disturbances.
5. The limited vertical extension of the disturbances is not considered.
6. Pressure gradients $\nabla\vec{P}$ are neglected.
7. The following approximations for the solid phase are made for the present three-phase bubbly flow model.
8. The vertical solid particle velocity (us,z) does not change with the disturbances.
9. The horizontal component of the solid phase (us,x) may occur due to the disturbances.
10. The solid holdup $\alpha$s is uniform in this modeled small region and remains constant with the disturbances.

With these assumptions, the disturbed state for the three-phase homogeneous flow can be characterized as follows

for liquid phase, $\vec{u}_l(x,y,z,t)=u_l(x,t)\vec{e}_z$, =
for bubble phase, $\vec{u}_b(x,y,z,t)=u_{b,z}\vec{e}_z+u_{b,x}\vec{e}_x$ and $\alpha_b\ (x,y,z,t)=\alpha_b(x,t)$,
for solid phase, $\vec{u}_s(x,y,z,t)=u_{s,z}\vec{e}_z+u_{s,x}\vec{e}$ and $\alpha_s\ (x,y,z,t)=\alpha^0_s$

Thus, the Navier–Stokes equation for the liquid phase in the three-phase bubble flow can be written as

$$\begin{aligned}&(1-\alpha_b-\alpha_s)\rho_l\left(\frac{\partial\vec{u}}{\partial t}+\vec{u}\cdot\nabla\vec{u}\right)\\&=-(1-\alpha_b-\alpha_s)\nabla\vec{P}+(1-\alpha_b-\alpha_s)\mu_l\Delta\vec{u}_l\\&+\frac{1}{3}(1-\alpha_b-\alpha_s)\mu_l\mathrm{grad}\,(\mathrm{div}\,\vec{u}_l)+\vec{F}\end{aligned}\tag{13}$$

Equation 13 be simplified to

$$(1-\alpha_b-\alpha_s)\rho_l\frac{\partial u_l}{\partial t}=(1-\alpha_b-\alpha_s)\mu_l\frac{\partial^2 u_l}{\partial x^2}-\Delta\rho g\tag{14}$$

As$\rho_l \gg \rho_b$, we have

$$\begin{aligned}\frac{\Delta\rho}{(1-\alpha_b-\alpha_s)\rho_l}&=\frac{(1-\alpha_b-\alpha_s-\Delta\alpha_b)\rho_l-(1-\alpha_b-\alpha_s)\rho_l}{(1-\alpha_b-\alpha_s)\rho_l}\\&=-\frac{\Delta\alpha_b}{1-\alpha_b-\alpha_s}\end{aligned}\tag{15}$$

Substituted Eq. 15 into Eq. 14, the N-S equation becomes

$$\frac{\partial u_l}{\partial t}=\nu_l\frac{\partial^2 u_l}{\partial x^2}+g\frac{\Delta\alpha_b}{1-\alpha_b-\alpha_s}\tag{16}$$

The continuity equation for the bubbles in the horizontal direction is

$$\frac{\partial\alpha_b}{\partial t}+\frac{\partial}{\partial x}u_{b,x}\alpha_b=0\tag{17}$$

Equations 16 and 17 are the N-S equation and continuity equation. An addition equation for the lateral force balance of the dispersed phases in the flow field is needed so that they can be solved identically.

*The Lateral Forces Acting on the Dispersed Phases (Bubbles and Solids).* To analyze the flow stability in the three-phase bubble column, both the dispersed phases (bubbles and solids) have to be considered. For gravity-driven vertical pipe flow, there are four lateral forces acting on the dispersed phases in the continuous liquid phase. They are

namely the turbulent dispersion force, virtual mass force, drag force, and transversal lift force.

For the turbulent dispersion force acting on a bubble or solid particle, an expression was derived by Burns et al.,[50] that is

$$\vec{F}_{\mathrm{TD}} = -\frac{3C_D v_t}{4d\mathrm{Pr}} u\rho_l \mathrm{grad}\,(\alpha) \tag{18}$$

Here $v_t$ is turbulent viscosity and Pr is the Prandtl number of liquid.

Tomiyama[40] suggested an empirical relation for the virtual mass force

$$\vec{F}_{\mathrm{VM}} = C_{\mathrm{VM}}\,\rho_l\left(\frac{d\vec{u}}{dt} - \frac{d\vec{u}_l}{dt}\right) \tag{19}$$

Here, the coefficient $C_{\mathrm{VM}} = 0.5$.

The drag force for the dispersion phase can be defined as

$$\vec{F}_D = \frac{3}{4d} C_D \rho_l |\vec{u} - \vec{u}_l|(\vec{u} - \vec{u}_l) \tag{20}$$

Equation 10 can be used to calculate $C_{\mathrm{D}}$ for the bubbles, and it shows that the sign of the drag force coefficient is always positive for bubbles. Equation 12 can be applied for the calculation of $C_{\mathrm{D}}$ for the solids.

The transversal lift force for a bubble or solids can be defined as

$$\vec{F}_{\mathrm{L}} = -C_{\mathrm{L}}\rho_l \alpha(\vec{u} - \vec{u}_l) \times \mathrm{curl}\,(\vec{u}_l) \tag{21}$$

where $\vec{F}_L$ is the lift force, $C_{\mathrm{L}}$ is the lift coefficient, The lift coefficient $C_{\mathrm{L}}$ determines the direction of bubble transport in the horizontal direction, and can either be positive or negative depending on the bubble size. Tomiyama[40] proposed a relationship based on their experimental investigations on a single bubble as follow

$$C_{\mathrm{L}} = \begin{cases} \min\left[0.288\tanh\left(0.121\mathrm{Re}\right), f(Eo_d)\right] & Eo_d < 4 \\ f(Eo_d) & \text{for} \quad 4 < Eo_d < 10 \\ 0.27 & Eo_d > 10 \end{cases} \tag{22}$$

with $f(Eo_d) = 0.00105Eo_d^3 - 0.0159Eo_d^2 - 0.0204Eo_d + 0.474$

It shows that the sign of the lift force coefficient is positive for small bubbles, but negative for large bubbles.

The transversal lift force acting on a solid particle in a slow shear flow is expressed as[51]

$$C_L = 0.51\log_{10}\mathrm{Re} - 0.22 + \frac{3}{16}(1 + 0.0045\mathrm{Re}) \tag{23}$$

It shows that the sign of the lift force coefficient is positive for $\mathrm{Re} > 1.158$.

Because both the bubbles and solid particles are dispersed in the continuous liquid phase, it is necessary to combine the solid phase with bubbles so as to analyze the three-phase flow field. The balance of the lateral forces for the dispersed phases can be given as

$$\begin{aligned} \vec{F}_{\mathrm{TD,b}}|_x + \vec{F}_{\mathrm{TD,s}}|_x + \vec{F}_{\mathrm{VM,b}}|_x + \vec{F}_{\mathrm{VM,s}}|_x + \vec{F}_{\mathrm{L,b}}|_x \\ + \vec{F}_{L,\mathrm{s}}|_x + \vec{F}_{D,\mathrm{b}}|_x + \vec{F}_{D,\mathrm{s}}|_x = 0 \end{aligned} \tag{24}$$

Noting that:

a. $\vec{F}_{\mathrm{VM,s}} = C_{\mathrm{VM}}\rho_l\left(\frac{d\vec{u}_{\mathrm{s}}}{dt} - \frac{d\vec{u}_l}{dt}\right)$ can be neglected, due to the small velocity difference between solid and liquid phase.

b. $\vec{F}_{\mathrm{TD,s}} = -\frac{3C_{D,\mathrm{s}}v_t}{4d_s\mathrm{Pr}} u_{\mathrm{s}}\rho_l \mathrm{grad}\,(\alpha_{\mathrm{s}}) = 0$, due to the uniform distribution of solid particles, $grad(\alpha_{\mathrm{s}})$ is zero.

Substituting Eqs. 18–21 into 24, the balance of the lateral forces becomes

$$\begin{aligned} &\alpha_{\mathrm{b}}(\rho_{\mathrm{b}} + C_{\mathrm{VM}}\rho_l)\left(\frac{\partial u_{\mathrm{b},x}}{\partial t} + u_{\mathrm{b}}\frac{\partial u_{\mathrm{b},x}}{\partial x}\right) + \frac{3C_{D,\mathrm{b}}}{4d_{\mathrm{b}}}\rho_l\alpha_{\mathrm{b}}u_{\mathrm{b},x}\sqrt{u_{\mathrm{b},z}^2 + u_{\mathrm{b},x}^2} \\ &+ \frac{3C_{D,\mathrm{s}}}{4d_{\mathrm{s}}}\rho_l\alpha_{\mathrm{s}}u_{\mathrm{s},x}\sqrt{u_{\mathrm{s},z}^2 + u_{\mathrm{s},x}^2} + C_{L,\mathrm{b}}\rho_l\alpha_{\mathrm{b}}u_{\mathrm{b},z}\frac{\partial u_l}{\partial x} + C_{L,\mathrm{s}}\rho_l\alpha_{\mathrm{s}}u_{\mathrm{s},z}\frac{\partial u_l}{\partial x} \\ &+ \frac{3C_{D,\mathrm{b}}}{4d_{\mathrm{b}}}\rho_l\frac{v_t}{\mathrm{Pr}}u_{\mathrm{b},z}\frac{1}{1-\alpha_{\mathrm{b}}}\frac{\partial\alpha_{\mathrm{b}}}{\partial x} = 0 \end{aligned} \tag{25}$$

Equations 16, 17, and 25 can now be used as the basic transfer functions to analysis the stability of the three-phase flow field.

*Transfer Function.* In this analysis, a disturbance, that is, an increase of the gas volume fraction $\delta\alpha_{\mathrm{b}}(x,t)$, happened in the three-phase flow field and the subsequent events are processed. The transfer procedure of the disturbance can be simplified as follow. The disturbance $\delta\alpha_{\mathrm{b}}(x,t)$ accelerates the liquid in vertical direction due to buoyancy, so that the disturbances of the liquid velocity $\delta u_l(x,t)\vec{e}_z$ and the gradient of the liquid velocity $\delta(\partial u_l/dx)(x,t)$ are generated. As Eq. 21 shows, the transversal lift force is proportional to the gradient of the liquid velocity $\delta(\partial u_l/dx)(x,t)$. The dispersed phases including bubbles and solid particles will start to migrate in the $x$ direction with the velocities $\delta u_{\mathrm{b}}(x,t)\vec{e}_x$ and $\delta u_{\mathrm{s}}(x,t)\vec{e}_x$, respectively. This migration may decrease the initial disturbance $\delta\alpha_{\mathrm{b}}(x)$ with a positive lift force coefficient or increase the initial disturbance $\delta\alpha_{\mathrm{b}}(x)$ with a negative lift force coefficient. In addition, according to the definition of the turbulent dispersion force shown in Eq. 18, the turbulent dispersion force always decreases the initial disturbance. For the disturbance, this transfer function can present a positive or negative feedback, which determines the stability of the disturbed three-phase flow field shown in Figure 16b.

In this analysis of the stability in a three-phase bubble column, the feedback of a small initial Dirac-shaped disturbance on itself is investigated. The basic transfer functions for the single effects can be obtained from the Eqs. 16, 17, and 25. Based on the automatic control theory,[52] the compact transfer functions can be derived by Laplace transform alter also. The system diagram of the feedback control loop in case of a homogeneous three-phase flow with monosized bubbles is shown schematically in Figure 17.

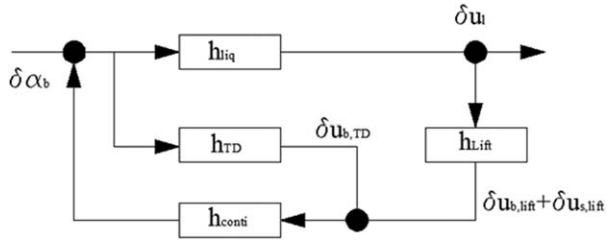


**Figure 17. Propagation and feedback of a disturbance $\delta\alpha_{\mathrm{b}}$.**

**The transfer function $h$ characterizes the output parameter of the disturbance.**

The transfer function $h_{\mathrm{Liq}}$ represents the variation of the liquid velocity as a consequence to the disturbance of the local gas volume fraction $\delta\alpha_{\mathrm{b}}$ and can be derived from the N-S equation of the liquid (Eq. 16). $h_{\mathrm{TD}}$ presents the change of the lateral bubble velocity caused by the local changer of the gas volume fraction due to the turbulent dispersion force, which can be deduced from the balance of forces acting on the dispersed phases in the lateral direction as Eq. 25. The transfer function $h_{\mathrm{Lift}}$ represents the variety of the lateral bubble velocity caused by the lateral lift force due to the variety of the gradients of the liquid velocity, and it can also be deduced by Eq. 25. Finally, $h_{\mathrm{Conti}}$ provides the modification of the local gas volume fraction caused by all the changes of the lateral bubble velocity, and it can be obtained from the continuity equation of the gas phase, as in Eq. 17. To obtain the feedback of a disturbance in the system as Figure 17 shown, Eqs. 16, 17, and 25 based on the undisturbed state are perturbed and applied to the Laplace transformation.

The $n$ waves single Fourier mode of the perturbation of the gas volume fraction $\Delta\alpha_{\mathrm{b}}(x,t)$ can be expressed as

$$\begin{aligned}\Delta\alpha_{\mathrm{b}}(x,t)&=\delta\tilde{\alpha}(t)\exp(inx)=\delta\tilde{\alpha}(t)(\cos(nx)+i\sin(nx))\\&=\delta\tilde{\alpha}_{re}(t)\cos(nx)+i\delta\tilde{\alpha}_{im}(t)\sin(nx)\end{aligned}\tag{26}$$

The wavy bar "$\sim$" represents the amplitude of the disturbance in the time domain. Equation 26 defines that the perturbation is periodic in space with frequency $n$. The disturbances of the liquid, bubbles, and solids velocities can be defined in the same way.

Substituting the disturbance $\Delta\alpha_{\mathrm{b}}(x,t)$ into Eq. 16, and applying the Laplace transform, the N-S equation (Eq. 16) for the disturbance can be simplified to

$$\mathrm{s}\delta u_l=-v_l n^2\delta u_l+g\frac{\delta\alpha_{\mathrm{b}}}{1-\alpha_{\mathrm{b}}^0-\alpha_{\mathrm{s}}}\tag{27}$$

The transfer function $h_{\mathrm{liq}}$ for the disturbance of the gas volume fraction on the vertical liquid velocity $u_{\mathrm{l}}$ in Laplacian space can be obtain

$$h_{\mathrm{Liq}}(\mathrm{s})=\frac{\delta u_l(\mathrm{s})}{\delta\alpha_{\mathrm{b}}(\mathrm{s})}=\frac{g}{(1-\alpha_{\mathrm{b}}^0-\alpha_{\mathrm{s}})(\mathrm{s}+v_l n^2)}\tag{28}$$

The continuity equation (Eq. 17) and the balance of lateral force equation (Eq. 25) have to be linearized for the deriving of transfer function. Due to the disturbances that are small comparing to the undisturbed value, the following expressions are used in Eqs. 17 and 25, $\alpha_{\mathrm{b}}=\alpha_{\mathrm{b}}^0+\Delta\alpha_{\mathrm{b}}$, as, $\Delta\alpha_{\mathrm{b}}<<\alpha_{\mathrm{b}}^0$, and writing for the constant undisturbed gas volume fraction $\alpha_{\mathrm{b}}^0$, simply use $\alpha_{\mathrm{b}}$ instead of $\alpha_{\mathrm{b}}^0$ from now:

$u_{\mathrm{l}}=\Delta u_{\mathrm{l}}$, because the undisturbed liquid velocity is zero. =

$u_{\mathrm{b}}=\Delta u_{\mathrm{b}}$, because the undisturbed bubble velocity in $x$ axis is zero.

$u_{\mathrm{s}}=\Delta u_{\mathrm{s}}$, because the undisturbed solids velocity in $x$ axis is zero.

Neglecting all terms with the disturbances of second order, the linearized continuity Eq. 17 becomes

$$\frac{\partial\Delta\alpha_{\mathrm{b}}}{\partial t}+\alpha_{\mathrm{b}}\frac{\partial\Delta u_{\mathrm{b}}}{\partial x}=0\tag{29}$$

In Laplacian space

$$\mathrm{s}\delta\alpha_{\mathrm{b}}-in\alpha_{\mathrm{b}}\delta u_{\mathrm{b}}=0\tag{30}$$

The transfer function $h_{\mathrm{conti}}$ can be reached

$$h_{\mathrm{conti}}=\frac{\delta\alpha_{\mathrm{b}}}{\delta u_{\mathrm{b}}}=\frac{-in\alpha_{\mathrm{b}}}{\mathrm{s}}\tag{31}$$

The linearized lateral force balance function of the dispersed phases, neglecting all terms with the disturbances of second order, becomes

$$\begin{aligned}&\alpha_{\mathrm{b}}(\rho_{\mathrm{b}}+C_{\mathrm{VM}}\rho_l)\frac{\partial u_{\mathrm{b}}}{\partial t}+\frac{3C_{D,\mathrm{b}}}{4d_{\mathrm{b}}}\rho_l\alpha_{\mathrm{b}}u_{\mathrm{b}}\Delta u_{\mathrm{b}}\\&+\frac{3C_{D,\mathrm{s}}}{4d_{\mathrm{s}}}\rho_l\alpha_{\mathrm{s}}u_{\mathrm{s}}\Delta u_{\mathrm{s}}+C_{L,\mathrm{b}}\rho_l\alpha_{\mathrm{b}}u_{\mathrm{b}}\frac{\partial\Delta u_l}{\partial x}+C_{L,\mathrm{s}}\rho_l\alpha_{\mathrm{s}}u_{\mathrm{s}}\frac{\partial\Delta u_l}{\partial x}\\&+\frac{3C_{D,\mathrm{b}}}{4d_{\mathrm{b}}}\rho_l\frac{v_t}{\mathrm{Pr}}u_{\mathrm{b}}\frac{1}{1-\alpha_{\mathrm{b}}}\frac{\partial\Delta\alpha_{\mathrm{b}}}{\partial x}=0\end{aligned}\tag{32}$$

Denoting

$$K_{\mathrm{Drag,b}}=\frac{3C_{D,\mathrm{b}}}{4d_{\mathrm{b}}}\frac{\rho_l}{\rho_{\mathrm{b}}+C_{\mathrm{VM}}\rho_l}u_{\mathrm{b}}$$

$$K_{\mathrm{Drag,s}}=\frac{3C_{D,\mathrm{s}}}{4d_{\mathrm{s}}}\frac{\alpha_{\mathrm{s}}}{\alpha_{\mathrm{b}}}\frac{\rho_l}{\rho_{\mathrm{b}}+C_{\mathrm{VM}}\rho_l}\mathrm{u_s}$$

$$K_{\mathrm{Lift,b}}=C_{L,\mathrm{b}}\frac{\rho_l}{\rho_{\mathrm{b}}+C_{\mathrm{VM}}\rho_l}u_{\mathrm{b}}$$

$$K_{\mathrm{Lift,s}}=C_{L,\mathrm{s}}\frac{\alpha_{\mathrm{s}}}{\alpha_{\mathrm{b}}}\frac{\rho_l}{\rho_{\mathrm{b}}+C_{VM}\rho_l}u_{\mathrm{s}}$$

$$K_{\mathrm{TD,b}}=K_{\mathrm{Drag,b}}\frac{v_t}{\mathrm{Pr}\,\alpha_{\mathrm{b}}(1-\alpha_{\mathrm{b}})}$$

The lateral force balance equation becomes

$$\begin{aligned}&\frac{\partial\Delta u_{\mathrm{b}}}{\partial t}+K_{\mathrm{Drag,b}}\Delta u_{\mathrm{b}}+K_{\mathrm{Drag,s}}\Delta u_{\mathrm{s}}+K_{\mathrm{Lift,s}}\frac{\partial\Delta u_l}{\partial x}\\&+K_{\mathrm{Lift},d}\frac{\partial\Delta u_l}{\partial x}+K_{\mathrm{TD,b}}\frac{\partial\Delta\alpha_{\mathrm{b}}}{\partial x}=0\end{aligned}$$

or

$$\begin{aligned}\frac{\partial\Delta u_{\mathrm{b}}}{\partial t}+K_{\mathrm{Drag,b}}\Delta u_{\mathrm{b}}=&-(K_{\mathrm{Lift,s}}+K_{\mathrm{Lift},d})\frac{\partial\Delta u_{\mathrm{l}}}{\partial x}\\&-K_{\mathrm{TD,b}}\frac{\partial\Delta\alpha_{\mathrm{b}}}{\partial x}-K_{\mathrm{Drag,s}}\Delta u_{\mathrm{s}}\end{aligned}\tag{33}$$

Inserting the disturbances into Eq. 33 and applying the Laplace transform

$$\begin{aligned}\mathrm{s}\delta u_{\mathrm{b}}+K_{\mathrm{Drag,b}}\delta u_{\mathrm{b}}=&-\mathrm{in}\,(K_{\mathrm{Lift,s}}+K_{\mathrm{Lift,d}})\\&\delta u_{\mathrm{l}}-inK_{\mathrm{TD,b}}\,\delta\alpha_{\mathrm{b}}-K_{\mathrm{Drag,s}}\,\delta u_{\mathrm{s}}\end{aligned}\tag{34}$$

The transfer function $h_{\mathrm{TD}}$ for a disturbance of the gas volume fraction on the horizontal gas velocity can be reached

$$h_{\mathrm{TD}}=\frac{\delta u_{\mathrm{b}}}{\delta\alpha_{\mathrm{b}}}=\frac{-inK_{\mathrm{TD,b}}}{\mathrm{s}+K_{\mathrm{Drag,b}}}\tag{35}$$

In the same way, the transfer function $h_{\mathrm{Lift}}$ for a disturbance of the vertical liquid velocity on the horizontal gas velocity can be deduced as

$$h_{\mathrm{Lift}}=\frac{\delta u_{\mathrm{b}}}{\delta u_{\mathrm{l}}}=\frac{-in\left(K_{\mathrm{Lift,b}}+K_{\mathrm{Lift,s}}\right)}{\mathrm{s}+K_{\mathrm{Drag,b}}} \tag{36}$$

Eqs. 28–35, and 36 are the transfer functions shown schematically in Figure 17.

*The Feedback for a Monosized Bubble System in Three-Phase Flow.* According to the theory of automatic control engineering, the transfer function for the total system shown in Figure 17 can be reached with a minus sign

$$\begin{aligned}H^{\mathrm{open}}&=-\left(h_{\mathrm{Liq}}h_{\mathrm{lift}}+h_{\mathrm{TD}}\right)h_{\mathrm{conti}}\\&=-\left(\frac{g}{\left(1-\alpha_{\mathrm{b}}^{0}-\alpha_{\mathrm{s}}\right)\left(\mathrm{s}+v_l n^2\right)}\frac{-in\left(K_{\mathrm{Lift,b}}+K_{\mathrm{Lift,s}}\right)}{\mathrm{s}+K_{\mathrm{Drag,b}}}+\frac{-inK_{\mathrm{TD,b}}}{\mathrm{s}+K_{\mathrm{Drag,b}}}\right)\left(\frac{-in\alpha_{\mathrm{b}}}{\mathrm{s}}\right)\\&=\frac{n\alpha_{\mathrm{b}}}{\mathrm{s}}\left(\frac{gn\left(K_{\mathrm{Lift,b}}+K_{\mathrm{Lift,s}}\right)}{\left(1-\alpha_{\mathrm{b}}^{0}-\alpha_{\mathrm{s}}\right)}\frac{1}{\left(\mathrm{s}+v_l n^2\right)\left(\mathrm{s}+K_{\mathrm{Drag,b}}\right)}+nK_{\mathrm{TD,b}}\frac{1}{\mathrm{s}+K_{\mathrm{Drag,b}}}\right)\end{aligned} \tag{37}$$

The transfer function (Eq. 37) has no imaginary part, which means that the feedback of the initial disturbance of the gas volume fraction on itself has the same spatial dependency as the initial disturbance itself. The feedback within the closed loop as shown in Figure 17 can, therefore, be given

$$H^{\mathrm{close}}=\frac{1}{1+H^{\mathrm{open}}}=\frac{\mathrm{s}\left(\mathrm{s}+v_l n^2\right)\left(\mathrm{s}+K_{\mathrm{Drag,b}}\right)}{\mathrm{s}^3+\left(K_{\mathrm{Drag,b}}+v_l n^2\right)\mathrm{s}^2+\left(K_{\mathrm{Drag,b}}v_l n^2+K_{\mathrm{TD,b}}\alpha_{\mathrm{b}}n^2\right)\mathrm{s}+K_{\mathrm{TD,b}}\alpha_{\mathrm{b}}n^4v_l+\frac{g}{1-\alpha_{\mathrm{b}}-\alpha_{\mathrm{s}}}n^2\alpha_{\mathrm{b}}\left(K_{\mathrm{Lift,b}}+K_{\mathrm{Lift,s}}\right)} \tag{38}$$

The stability condition for the closed-loop transfer function is that all the poles, that is, the roots of the characteristic polynomial $1+H^{\mathrm{open}}$, have negative real parts. According to the automatic control theory, the Routh–Hurwitz criterion can be used to determine the stability condition.[52] This criterion states that the system will be stable, if all the coefficients of the characteristic equation $1+H^{\mathrm{open}}$ and Hurwitz determinants are positive.

The characteristic equation is equivalent to that the denominator of the right side of Eq. 38 to be zero

$$\begin{aligned}&\mathrm{s}^3+\left(K_{\mathrm{Drag,b}}+v_l n^2\right)\mathrm{s}^2+\left(K_{\mathrm{Drag,b}}v_l n^2+K_{\mathrm{TD,b}}\alpha_{\mathrm{b}}n^2\right)\mathrm{s}\\&+K_{\mathrm{TD,b}}\alpha_{\mathrm{b}}n^4v_l+\frac{g}{1-\alpha_{\mathrm{b}}-\alpha_{\mathrm{s}}}n^2\alpha_{\mathrm{b}}\left(K_{\mathrm{Lift,b}}+K_{\mathrm{Lift,s}}\right)=0\end{aligned} \tag{39}$$

The coefficients of the characteristics polynomial can be derived

$$\sim\mathrm{s}^3: a_3=1>0,$$

$$\sim\mathrm{s}^2: a_2=K_{\mathrm{Drag,b}}+v_l n^2>0, \text{ according to the definitions,}$$

$$\sim\mathrm{s}^1: a_1=K_{\mathrm{Drag,b}}v_l n^2+K_{\mathrm{TD,b}}n^2\alpha_{\mathrm{b}}>0, \text{ according to the definitions,}$$

$$\sim 1: a_0=K_{\mathrm{TD,b}}n^4\alpha_{\mathrm{b}}v_{\mathrm{l}}+\frac{g}{1-\alpha_{\mathrm{b}}-\alpha_{\mathrm{s}}}n^2\alpha_{\mathrm{b}}\left(K_{\mathrm{Lift,b}}+K_{\mathrm{Lift,s}}\right), \tag{40}$$

$a_0>0$ is one condition for stability!

Hurwitz determinants should be larger than zero, which is

$$\begin{aligned}&a_2a_1-a_3a_0=\\&\left(K_{\mathrm{Drag,b}}+v_l n^2\right)\left(K_{\mathrm{Drag,b}}v_l n^2+K_{\mathrm{TD,b}}n^2\alpha_{\mathrm{b}}\right)\\&-K_{\mathrm{TD,b}}n^4\alpha_{\mathrm{b}}v_{\mathrm{l}}-\frac{g}{1-\alpha_{\mathrm{b}}-\alpha_{\mathrm{s}}}n^2\alpha_{\mathrm{b}}\left(K_{\mathrm{Lift,b}}+K_{\mathrm{Lift,s}}\right)>0\end{aligned} \tag{41}$$

Equation 41 determines the upper limit of the lift force coefficient $C_{\mathrm{L}}$ for the bubbles. For practical cases, the $C_{\mathrm{L}}$ cannot reach this upper limit (positive value), so that the Hurwitz determinants is not relevant to this analysis. Finally, the only criterion for this stability analysis is $a_0>0$, which reads

$$\begin{aligned}&K_{\mathrm{TD,b}}n^4\alpha_{\mathrm{b}}v_{\mathrm{l}}+\frac{g}{1-\alpha_{\mathrm{b}}-\alpha_{\mathrm{s}}}n^2\alpha_{\mathrm{b}}\left(K_{\mathrm{Lift,b}}+K_{\mathrm{Lift,s}}\right)\\&=\frac{3C_{\mathrm{D,b}}}{4d_{\mathrm{b}}}\frac{\rho_{\mathrm{l}}}{\rho_{\mathrm{b}}+C_{\mathrm{VM}}\rho_l}u_{\mathrm{b}}\frac{v_{\mathrm{t}}}{\mathrm{Pr}\,\alpha_{\mathrm{b}}\left(1-\alpha_{\mathrm{b}}\right)}\alpha_{\mathrm{b}}n^4v_l\\&+\frac{g}{1-\alpha_{\mathrm{b}}-\alpha_{\mathrm{s}}}n^2\alpha_{\mathrm{b}}\left(C_{\mathrm{L,b}}\frac{\rho_l}{\rho_{\mathrm{b}}+C_{\mathrm{VM}}\rho_l}u_{\mathrm{b}}+C_{\mathrm{L,s}}\frac{\alpha_{\mathrm{s}}}{\alpha_{\mathrm{b}}}\frac{\rho_l}{\rho_{\mathrm{b}}+C_{\mathrm{VM}}\rho_l}u_{\mathrm{s}}\right)>0\end{aligned} \tag{42}$$

Equation 42 reaches

$$C_{\mathrm{L,b}}>-\left(\frac{1-\alpha_{\mathrm{b}}-\alpha_{\mathrm{s}}}{1-\alpha_{\mathrm{b}}}\frac{3C_{\mathrm{D,b}}v_{\mathrm{t}}v_{\mathrm{l}}n^2}{4d_{\mathrm{b}}g\mathrm{Pr}\,\alpha_{\mathrm{b}}}+C_{\mathrm{L,s}}\frac{u_{\mathrm{s}}}{u_{\mathrm{b}}}\frac{\alpha_{\mathrm{s}}}{\alpha_{\mathrm{b}}}\right) \tag{43}$$

Burns et al.[50] reported the turbulent Prandtl number Pr is in the order of unity, and Sato et al.[53] suggested

$$v_t=0.6\alpha_{\mathrm{b}}d_{\mathrm{b}}u_{\mathrm{b}} \tag{44}$$

As mentioned before, $n$ is the spatial frequency of the disturbance. Define a typical length scale for the possible disturbances $L$

$$n=\frac{\pi}{L} \tag{45}$$

Substituted Eqs. 44 and 45 into Eq. 43, the criterion for the stability for a homogeneous three-phase flow field with monosized bubbles can be obtained

$$C_{L,\mathrm{b}}>-\left(\frac{1-\alpha_{\mathrm{b}}-\alpha_{\mathrm{s}}}{1-\alpha_{\mathrm{b}}}4.44\frac{C_{D,\mathrm{b}}u_{\mathrm{b}}v_l}{gL^2}+C_{L,\mathrm{s}}\frac{u_{\mathrm{s}}}{u_{\mathrm{b}}}\frac{\alpha_{\mathrm{s}}}{\alpha_{\mathrm{b}}}\right) \tag{46}$$

*Simplified Analysis for N Bubble Size Classes System.* According to Lucas et al.,[49] the stabilizing action of the turbulent dispersion $\vec{F}_{TD}$ is very weak comparing to the effects

of the lift force and drag force. As shown in Figure 17, the transfer function of the system without the turbulent dispersion can be written as

$$H^{\text{open}} = -h_{\text{Liq}}\, h_{\text{lift}}\, h_{\text{conti}} \tag{47}$$

The simplified analysis for $N$ bubble size classes can be carried out with neglecting the turbulent dispersion. The transfer of the $N$ bubble size classes can be represented by

$$\begin{pmatrix} \delta\alpha'_{\text{b},1} \\ \vdots \\ \delta\alpha'_{\text{b,n}} \end{pmatrix} = -\begin{pmatrix} H_1^{\text{open}} \ldots H_1^{\text{open}} \\ \vdots\,\vdots \\ H_N^{\text{open}} \ldots H_n^{\text{open}} \end{pmatrix} \begin{pmatrix} \delta\alpha_{\text{b},1} \\ \vdots \\ \delta\alpha_{\text{b,n}} \end{pmatrix}$$
$$= \begin{pmatrix} h_{\text{Liq}}\, h_{\text{lift},1} h_{\text{conti},1} \ldots\ldots h_{\text{Liq}}\, h_{\text{lift},1} h_{\text{conti},1} \\ \vdots\,\vdots \\ h_{\text{Liq}}\, h_{\text{lift},N} h_{\text{conti},N} \ldots\ldots h_{\text{Liq}}\, h_{\text{lift},N} h_{\text{conti},N} \end{pmatrix} \times \begin{pmatrix} \delta\alpha_{\text{b},1} \\ \vdots \\ \delta\alpha_{\text{b},n} \end{pmatrix} \tag{48}$$

The closed loop transfer function for all $N$ groups bubbles becomes

$$1 - \sum_{i=1}^{N} H^{\text{open}} = 1 + \sum_{i=1}^{N} h_{\text{Liq}}\, h_{\text{lift}}\, h_{\text{conti}} = 0 \tag{49}$$

Inserting Eqs. 28, 31, and 36 into Eq. 49

$$\text{s}\left(\text{s} + v_l n^2\right) \prod_{i=1}^{N} \left(\text{s} + K^i_{\text{Drag,b}}\right)$$
$$+ \frac{g n^2}{1 - \alpha_{\text{b}} - \alpha_{\text{s}}} \sum_{i=1}^{N} \left( \alpha_{\text{b},i} \left( K^i_{\text{Lift,b}} + K^i_{\text{Lift,s}} \right) \prod_{j \neq i} \left( \text{s} + K^j_{\text{Drag,b}} \right) \right) = 0 \tag{50}$$

Equation 34 is a polynomial of $N+2$ order, and the criterion $a_0 > 0$ can be obtained

$$\sum_{i=1}^{N} \alpha_{\text{b}}^i \frac{K^i_{\text{Lift,b}} + K^i_{\text{Lift,s}}}{K^i_{\text{Drag,b}}} > 0$$

or

$$\sum_{i=1}^{N} d_{\text{b},i} \alpha_{\text{b},i} \frac{\alpha_{\text{b}}{}^2 u_{\text{b},i} C^i_{L,\text{b}} + \alpha_{\text{b},i} \alpha_{\text{s}} u_{\text{s}} C_{\text{L,s}}}{C^i_{\text{D,b}}} > 0 \tag{51}$$

Equation 51 is the approximated stability criterion for the effect of the lift force, with neglected turbulent dispersion and $N$ classes bubble size in a homogenous three-phase flow. With the solid phase holdup $\alpha_{\text{s}} = 0$, Eq. 51 becomes the criterion for the two-phase bubbly flow. On the other side, with $N = 1$, it becomes the results for the monosized bubble system, Eq. 46 with vanishing turbulent viscosity

$$C_{\text{L,b}} + C_{\text{L,s}} \frac{u_{\text{s}}}{u_{\text{b}}} \frac{\alpha_{\text{s}}}{\alpha_{\text{b}}} > 0 \tag{52}$$

The lift force coefficient for bubbles may be positive (small bubbles) or negative (large bubbles). According to the above feedback mechanism for a small disturbance happened on the local air volume fraction, the small bubbles stabilize the flow while the large bubbles lead to unstable gas fraction distributions. Equation 51 also shows that the solid phase has an important effect to the stability of a homogeneous three-phase flow. As mentioned before, the lift force coefficient for the solid phase is positive for $\text{Re} > 1.158$ which happens to almost all situations in three-phase flow. It also suggests that the solid phase almost always stabilizes the flow filed when the solid phase velocity $u_{\text{s}}$ has the same direction as the bubble velocity $u_{\text{b}}$, and it destabilizes the flow field with an opposite velocity of $u_{\text{b}}$.

*Comparison with the Experimental Results (Homogeneous Regime).* Equation 51 can be used to compare with the results of the PDA measurements presented earlier. At any particular measurement location, the number of the valid signal from bubbles is denoted as $N$. $\alpha_{\text{b}}$ is the local bubble volume fraction calculated from all measured bubble signals, which can be obtained by Eq. 7. $\alpha_{\text{s}}$ is the local solids holdup for all measured solid particle signals, and can be obtained by the same equation with $d_i = 3$ mm, because the solid particles has an unique diameter of 3 mm. Following Eq. 7, $\alpha_{\text{b}}^i$ can be obtained by

$$\alpha_{\text{b}}^i = \frac{\pi}{6} \frac{1}{\Delta t} \frac{d_{\text{b},i}}{|\vec{U}_{\text{b},i}|} \frac{1}{A_{pv,i}} \tag{53}$$

$u_{\text{b},i}$ is the single bubble velocity, and $u_{\text{s}}$ is the time-averaged solid-phase velocity.

$$\text{Denoting}: k = \sum_{i=1}^{N} d_{\text{b},i} \alpha_{\text{b},i} \frac{\alpha_{\text{b}}{}^2 u_{\text{b},i} C^i_{L,\text{b}} + \alpha_{\text{b},i} \alpha_{\text{s}} u_{\text{s}} C_{L,\text{s}}}{C^i_{D,\text{b}}} \tag{54}$$

Hence, $k > 0$ corresponds to a steady homogeneous bubbly flow. It is also suitable for the two-phase bubbly flow with $\alpha_{\text{s}} = 0$.

The calculated results of $k$ for the mean gas volume fraction 1.68% (air flow rate 0.8 L/min) at two different heights $z = 200$ and 400 mm are shown in Figure 18. It shows that the steady criterion, $k > 0$, is satisfied at all points inside the flow field, which agrees well with the observed phenomena that the bubble plume flow was steady in the three-phase bubble column. The corresponding case for the unstable

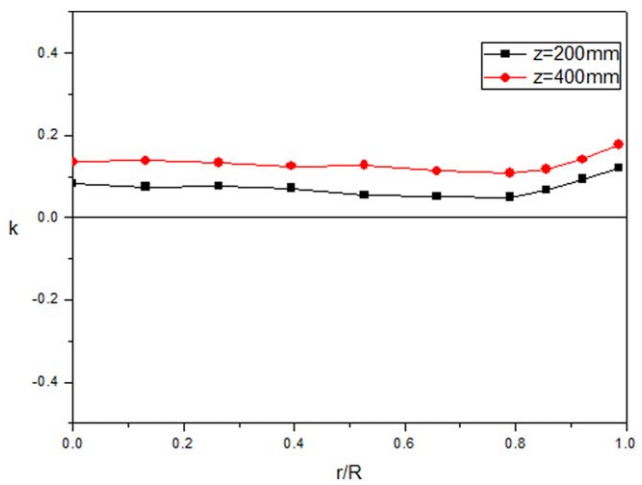


**Figure 18. The criterion *k* (Eq. 54) for the mean gas volume fraction 1.68% (air flow rate 0.8 L/min) at two different heights *z* = 200 and 400 mm in the three-phase bubble column.**

**[Color figure can be viewed in the online issue, which is available at wileyonlinelibrary.com**

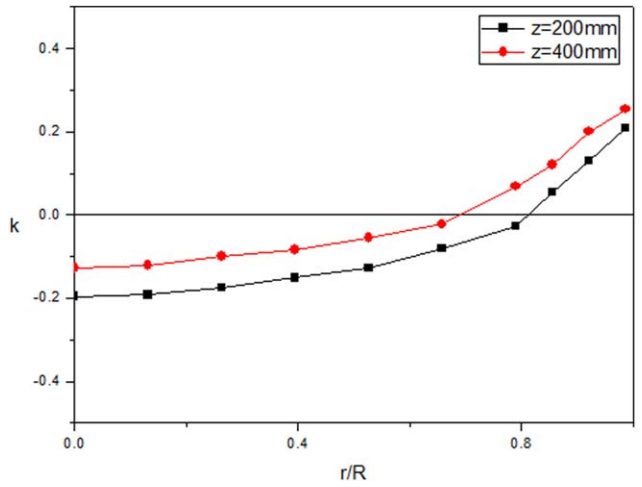


**Figure 19. The criterion *k* (Eq. 54) for the mean gas volume fraction 1.68% (air flow rate 0.8 L/min) at two different heights *z* = 200 and 400 mm in the two-phase bubble column.**

**[Color figure can be viewed in the online issue, which is available at wileyonlinelibrary.com.]**

bubble plume in a two-phase bubble column with the same condition is shown in Figure 19.

Figure 19 shows a typical unsteady bubbly flow, except the points near the wall, the criterion $k > 0$ cannot be satisfied. The reason for the steady flow structure near the wall may be due to the fact that only small bubbles can arrive in those locations with a positive lift force coefficient. The overall flow field for the two-phase bubble column is unstable. An occasional increase of the air volume fraction will lead to the collapse of the stability, so that the bubble plume has to meander in the bubble column. With added solid particles, the bubble plume flow behavior can be modified. Noting that for the solid phase, their lift force coefficient would always be positive, and it moves upward with the bubbles at the center region while moves downward near the wall. Figure 18 shows an obvious increase of the value of $k$ at all locations except near the wall. The bubble flow is stabilized at the center region. It also shows that the value $k$ is slightly decreased at the points near the wall due to the negative velocity of the solids, but the value of $k$ is still larger than zero and the flow field remains stable. On the whole, the flow field is stabilized with the added solid phase as shown in Figure 18.

Further measurements also reinforced our analysis that the added solid particle can increase the stability according to the criterion at centerline and stabilize the bubble plume flow. With the same setup for the mean gas volume fraction 1.68% (air flow rate 0.8 L/min) but different solid-phase volume fractions, the value of criterion $k$ at $r/R = 0$ can be calculated by the results of PDA measurements. It was clear that the value of $k$ increased with the solid-phase volume fraction as shown in Figure 20.

The above analysis has shown that the criterion on the stability of the three-phase flow can be used to explain the above experiment data well. However, the air flow rates used in above experiments are relatively low and represent only the flow in homogeneous regime.

*Further Investigation for the Transition and Heterogeneous Bubble Column Regime.* Homogeneous and heterogeneous flow field are two different flow regimes, one important distinction is the absence or presence of the unsteady large scale vortical motion of bubbly mixture. This coherent flow structures develop gradually with the increased air flow rate, which means that there is a transition regime between the homogeneous and heterogeneous flow regime. To verify the above analysis, further experiments have been performed at air flow rates 2.0 L/min for the transition regime and 4.0 L/m for the heterogeneous regime.

For PDA measurements in the transition or the heterogeneous flow field in a bubble column, the difficulty is to distinguish solid phase and bubbles from the signals. In our measurements of the bubble column in homogeneous regime, the diameters of the generated bubbles were controlled and it was always smaller than the solid particles, so that it is easy to distinct the signals from bubbles or solid particles by the diameter information. However, as soon as the unsteady vortex of the bubbly flow appears in the heterogeneous or transition regime bubbly flow field, there are possibilities of bubbles coalescence in this region, which may produce many bubbles larger than the solid particles. The size range of the solids is covered by the size range of bubbles. It is impossible to distinguish the signals between solids and bubbles with the signal size any more.

Here, the information of the velocity difference between the signals of bubbles and solid were applied to distinguish the bubbles and solids for the measurements of relative higher flow rates. As Figure 2b shows, all the signals of solids measured by PDA has a range from 2.8 to 3.2 mm, for each measured points for the transition and heterogeneous case, only the signals in this size range were the mixture of the signals from solids and bubbles. The velocity distribution for all the signals in the size range of 2.8 to 3.2 mm at $z = 600$ mm and at air flow rate 4.0 L/min is shown in Figure 21.

Figure 21 shows that the signals velocity distribution with the size range of 2.8–3.2 mm consisted of two distinct peaks. As shown in Figure 11, the bubbles velocity was obviously higher than the solids velocity. On the other hand, Figure 12 shows that the bubbles velocity increases with the bubble size, so that a 3 mm bubble should have a velocity larger

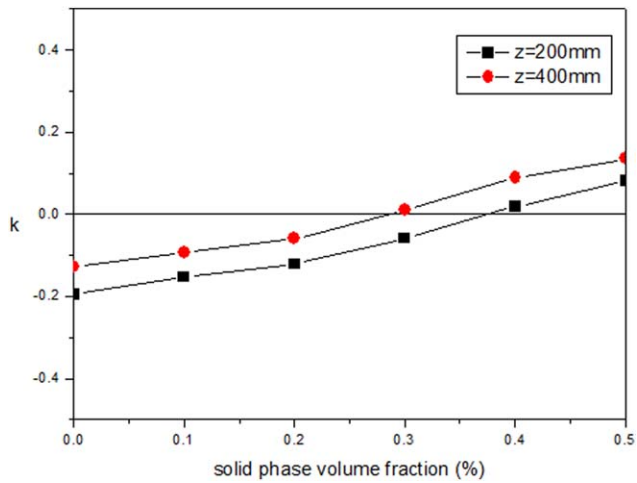


**Figure 20. The criterion *k* for the mean gas volume fraction 1.68% (air flow rate 0.8L/min) at *r/R* = 0 with different solid phase holdup in the three-phase bubble column.**

**[Color figure can be viewed in the online issue, which is available at wileyonlinelibrary.com.]**

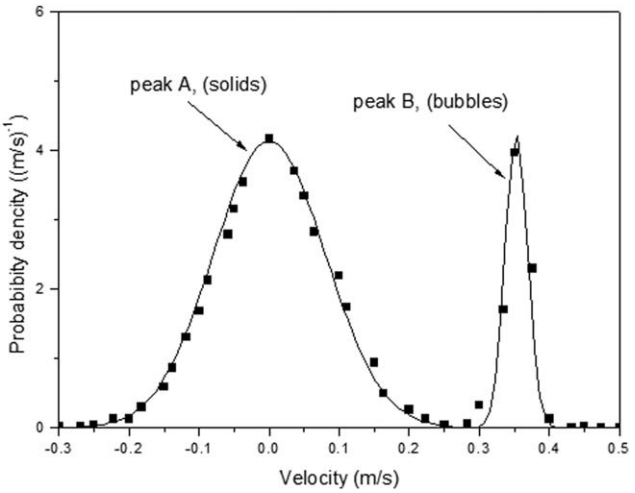


**Figure 21. The velocity distribution with the size range of 2.8–3.2 mm for all the measurement points at $z = 600$ mm and at air flow rate 4.0 L/min.**

than 0.2 m/s. It is a reasonable speculation that the peak B in Figure 21 was almost from the signals of bubbles and the peak A which had relative lower velocities represented the solids. The two peaks are distinctive so that we can use this velocity information to differentiate the solids and bubbles in the measurements of the transition and heterogeneous regime bubble column.

Using above method, the experimental data can be applied to the analysis and the criterion $k$ can be calculated for the measurements at relative higher air flow rates. The calculated results of $k$ for the air flow rate 2.0 L/min at two different heights $z = 200$ and 400 mm are shown in Figure 22.

Figure 22 shows a typical $k$ value distribution for the transition regime. The $k$ is larger than zero except the centerline region, which means that the flow field was quasihomogeneous but with some fluctuation near the centerline. It is corresponding to the experimental phenomena that sometimes there appeared several larger bubbly vortexes in the stable bubble column. The vortexes caused the coalescence of the bubbles, and according to Eq. 22, the bigger bubbles will cause a negative lift force which is the reason of the unstable flow field. It should be noted that this vortexes have to first appear at the center region due to the present setup of the bubble generator. The region away from the center will unavoidable be affected by this vorticities too. The propagation and feedback of the disturbance will happen at the adjacent region as shows in Figure 17. According to our previous analysis, the region away from the centerline can still remain in the homogeneous regime due to the $k$ value is larger than zero and it remains a negative feedback for the transfer function in Figure 17.

When the air flow rate increased to 4.0 L/min, the flow field is totally heterogeneous in the bubble column. The calculated results of $k$ for the air flow rate 4.0 L/min at two different heights $z = 200$ and 400 mm are shown in Figure 23.

Figure 23 shows that the $k$ value is negative at almost all measurement points at 4.0 L/min, which is corresponding to the fact that the flow field is chaotic and the bigger bubbles appear in random due to the coalescence. Similar to the heterogeneous case of the two-phase bubble column shown in Figure 19, the $k$ values are positive near the wall. The reason may be that the small bubbles tend to move to the wall and the coalescence is relative hard to happen there. This figure also shows that, at air flow rate 4.0 L/min, the higher gas volume fraction make the system more vulnerable to the disturbance. The onset of the coalescence will trigger the domino effect of the whole bubble column. The bigger bubbles will quickly change the $k$ value to negative, as shown in Figure 23, and the whole bubble column turns to the heterogeneous regime.

In short, the investigations presented here have shown that the analysis on the stability of the three-phase flow can be used to explain the homogeneous transition and heterogeneous regime of the three-phase bubble column. The detailed PDA measurements of the three-phase bubble column reinforce this analysis and it also proved that the criterion $k$ (Eq.

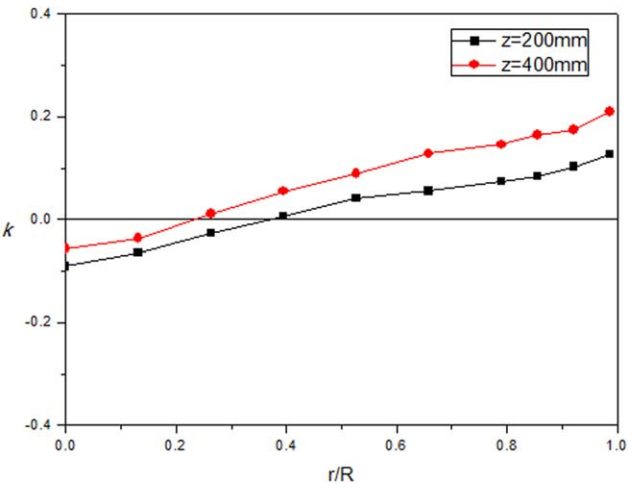


**Figure 22. The criterion $k$ (Eq. 54) for the air flow rate 2.0 L/min at two different heights $z = 200$ and 400 mm in the three-phase bubble column.**

**[Color figure can be viewed in the online issue, which is available at wileyonlinelibrary.com.]**

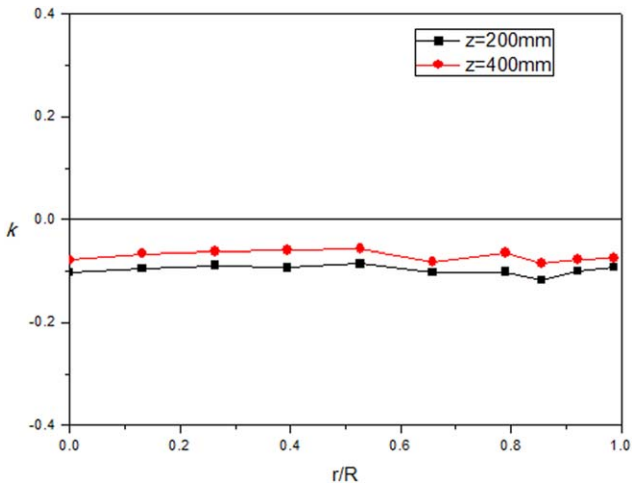


**Figure 23. The criterion $k$ (Eq. 54) for the air flow rate 4.0 L/min at two different heights $z = 200$ and 400 mm in the three-phase bubble column.**

**[Color figure can be viewed in the online issue, which is available at wileyonlinelibrary.com.]**

54) can be used to estimate the flow regime of the bubble column. The small bubbles and relative lower air flow rate maintain the bubble column in the homogeneous regime with positive $k$ value in the whole bubble column. As the air flow rate increase, the bubbles coalescence appears and the $k$ begin to show negative value at a small center regime, which means that the flow field has transform to the transition regime. Finally, the higher air flow rate will trigger the bubble column to heterogeneous regime. The onset of strong coalescence destabilizes the total flow field, and the bigger bubbles are generated all over the bubble column. The $k$ values become minus in the entire bubble column except near the wall.

## Concluding Remarks

A three-phase bubble column with a point air source centrally mounted at the bottom was investigated by PDA to obtain the simultaneous nonintrusive and instantaneous measurements of the air, liquid, and solid phase velocities as well as the bubble size. The three-phase flow fields at three different air rates 0.4, 0.8, and 1.2 L/min (corresponding to the mean gas volume fractions of 0.0048, 0.0168, and 0.0227, respectively) were investigated, respectively, for the homogeneous bubble column regime. The point air source resulted in a jet effect at $z = 50$ mm, and a stable large scale circulation pattern including both solid and liquid phase for all three cases. The detailed spatial distributions of liquid, bubble, and solid phase were presented.

The flow fields of the air and liquid phase were relatively more stable than that of the two-phase bubble column, which had bimodal probability density distributions for both liquid and bubble velocities. A new stability criterion was proposed for the three-phase bubble columns by applying the automatic control theory. By considering the drag and lift forces acting on the solid phase, it was found that the criterion was able to predict the stability of the overall flow behavior inside the column, and it concluded that the solid phase was the cause of stability with the lower solid-phase volume fraction (up to 1.2%) in our investigation.

Further investigation for the transition and the heterogeneous bubble column regime at air rates 2.0 and 4.0 L/min shown that this criterion can also be used as a general prediction of flow stability in this three-phase bubble column. Overall, the results from this study can improve the understanding of the flow behavior in a three-phase bubble column with a bottom-mounted point air source for environmental applications.

## Notation

$a$ = constant coefficient for polynomial
$A$ = ratio of mean bubble velocity squared to the bubble velocity variance, m/s
$A_{col}$ = cross-sectional of bubble column, $m^2$
$A_{pv}$ = area of prove volume cross-section, $m^2$
$A_{spa}$ = area of sparger, $m^2$
$c_{v,g}$ = volume concentration of gas, %
$C_d$ = drag coefficient
$C_L$ = lift coefficient
$C_{VM}$ = coefficient of virtual mass force
$d$ = diameter, m
$D$ = diameter of the bubble column, m
$e$ = unit vector
$E_o$ = Eotovs number
$f$ = focal length, m
$f'$ = effective focal length, m
$F$ = force, N
$g$ = gravitational acceleration, m/s$^2$
$h$ = transfer function
$H$ = initial liquid level in bubble column, m
$i$ = imaginary unit
$k$ = stability criterion
$K$ = constant symbol
$m$ = refractive index
$P$ = pressure, Pa
$Pr$ = Prandtl number
$q$ = Gaussian distribution
$Q_G$ = volume flow rate of gas, m$^3$/s
$R_e$ = Reynolds number of a bubble
$r$ = radial position, m
$R$ = radius, m
$t$ = time, s
$T$ = velocity variance, m/s
$u,v$ = velocity, m/s
$U$ = the measured velocity of signal, m/s
$V_G$ = superficial gas velocity, m/s
$V_t$ = terminal velocity, m/s
$x,y,z$ = Cartesian coordinates, m

### *Greek letters*

$\alpha$ = volume fraction
$\nu$ = kinematic viscosity, m$^2$/s
$\rho$ = density, kg/m$^3$
$\sigma$ = surface tension, N/s
$\delta$ = perturbation
$\nu$ = kinematic viscosity, m$^2$/s
$\mu$ = viscosity, Pa s

### *Subscripts*

0 = centerline
1 = air
2 = glass
3 = liquid
$b$ = bubble
conti = continuity equation
close = close loop
D, Drag = drag force
$g$ = gas
$s$ = solid
$l$,Liq = liquid
$L$,Lift = lift force
open = open loop
s = solid
TD = turbulence dispersion
t = turbulence
VM = virtual mass force
$w$ = wall
$\infty$ = terminal velocity

## Literature Cited


1. Shah YT, Kelkar BG, Godbole SP, Deckwer WD. Design parameters estimations for bubble column reactors. *AIChE J*. 1982;28(3):353–379.
2. Fan LS. Gas–Liquid–Solid Fluidization Engineering. Stoneham: Butterworth, 1989.
3. Chen J, Kemoun A, Al-Dahhan MH, Dudukovic MP, Lee DJ, Fan LS. Comparative hydrodynamics study in a bubble column using computer-automated radioactive particle tracking (CARPT)/computed tomography (CT) and particle image velocimetry (PIV). *Chem Eng Sci*. 1999;54(13–14):2199–2207.
4. Mudde RF. Gravity-driven bubbly flows. *Ann Rev Fluid Mech*. 2005;37:393–423.

5. Tang CZ, Heindel TJ. Gas-liquid-fiber flow in a cocurrent bubble column. *AIChE J*. 2005;51(10):2665–2674.
6. Ge W, Chen F, Gao J, Gao S, Huang J, Liu X, Ren Y, Sun Q, Wang L, Wang W, Yang N, Zhang J, Zhao H, Zhou G, Li J. Analytical multiscale method for multiphase complex systems in process engineering—bridging reductionism and holism. *Chem Eng Sci*. 2007;62:3346–3377.
7. Yang GQ, Du B, Fan LS. Bubble formation and dynamics in gas–liquid–solid fluidization—A review. Chem Eng Sci. 2007;62(1):2–27. Available at: http://www.sciencedirect.com.ezlibproxy1.ntu.edu.sg/science?_ob=ArticleURL&_udi=B6TFK-4KRFV4D-1&_user=892051&_coverDate=01%2F31%2F2007&_rdoc=3&_fmt=high-_orig=browse&_srch=doc-info%28%23toc%235229 %232007%23999379998%23637663%23FLA%23display%23Volume%29&_cdi=5229&_sort=d&_docanchor= &_ct=55&_acct=C000047479&_version=1&_urlVersion=0&_userid= 892051&md5=af19f26dcdbc0cd49abe838d14150c7b.
8. Liu L, Sheng GP, Li WW, Zeng RJ, Yu HQ. Experimental and numerical analysis of the hydrodynamic behaviors of aerobic granules. *AIChE J*. 2011;57(10):2909–2916.
9. Groen JS, Oldeman RGC, Mudde RF, Van Den Akker HEA. Coherent structures and axial dispersion in bubble column reactors. *Chem Eng Sci*. 1996;51:2511–2520.
10. Yang N, Chen J, Ge W, Li J. A conceptual model for analyzing the stability condition and regime transition in bubble columns. *Chem Eng Sci*. 2010;65(1):517–526.
11. Warsito W, Fan LS. Dynamics of spiral bubble plume motion in the entrance region of bubble columns and three-phase fluidized beds using 3D ECT. *Chem Eng Sci*. 2005;60(22):6073–6084.
12. Joshi JB, Lali AM. Velocity-holdup relationship in multiphase contactors—a unified approach. *Front Chem React Eng*. 1984;1:314–329.
13. Bachalo WD, Houser MJ. *Development of the phase Doppler spray analyzer for liquid drop size and velocity characterizations*. In: 20th Joint Propulsion Conference June 11–13. Cincinnati, Ohio: AIAA, 1984:1199.
14. Domnick J, Lindenthal A, Tropea C, Xu TH. Application of phase Doppler anemometry in paint sprays. *Atomization Sprays*. 1994;4:437–450.
15. Wang P, Yu SCM, Ng HW. Particle velocities, sizes and flux distribution in plasma spray with two powder injection ports. *Mater Sci Eng A*. 2004;383(1):122–136.
16. Braeske H, Brenn G, Domnick J, Durst F, Melling A, Ziema M. Extended phase-Doppler anemometry for measurements in three-phase flows. *Chem Eng Technol*. 1998;21:415–420.
17. Lain S, Bröder D, Sommerfeld M. Experimental and numerical studies of the hydrodynamics in a bubble column. *Chem Eng Sci*. 1999;54(21):4913–4920.
18. Brenn G, Braeske H, Durst F. Investigation of the unsteady two-phase flow with small bubbles in a model bubble column using phase-Doppler anemometry. *Chem Eng Sci*. 2002;57(24):5143–5159.
19. Gan ZW, Yu SCM, Law AWK. Hydrodynamic stability of a bubble column with a bottom-mounted point air source. *Chem Eng Sci*. 2011;66(21):5338–5356.
20. Tay JH, Liu QS, Liu Y. The effects of shear force on the formation, structure and metabolism of aerobic granules. *Appl Microbiol Biotechnol*. 2001;57(1–2):227–233.
21. Liu Y, Tay JH. State of the art of biogranulation technology for wastewater treatment. *Biotechnol Adv*. 2004;22(7):533–563.
22. Hughes RR, Handles AE, Evans HD, Maycock RL. The formation of bubbles at simple orifices. *Chem Eng Prog*. 1955;51:557–563.
23. Liow JL, Quasi-equilibrium bubble formation during top-submerged gas injection. *Chem Eng Sci*. 2000;55(20):4515–4524.
24. Hsu CH, Chen PC, Kung KY. Lai C. Impacts of ratio of asymptotic bubble width to diameter of circular tube and Reynolds number in a gas bubble driven. *Chem Eng Sci*. 2005;60(19):5341–5355.
25. Joshi JB, Parasu VU, Prasad ChV, Phanikumar DV, Deshpande NS, Thakare SS, Thorat BN. Gas hold-up structure in bubble column reactors. *Proc Indian Natl Sci Acad*. 1998;64A(4):441–567.
26. Bhole MR, Roy S, Joshi JB. Laser Doppler anemometer measurements in bubble column: effect of sparger. *Ind Eng Chem Res*. 2006;45(26):9201–9207.
27. Richardson JF, Zaki WN. Sedimentation and fluidisation: Part 1. *Trans Inst Chem Eng*. 1954;32:35–53.
28. Ishii M, Zuber N. Drag and relative velocity in bubbly, droplet or particulate flows. *AIChE J*. 1979;25:843–855.
29. Zenit R, Koch DL, Sangani AS. Measurements of the average properties of a suspension of bubbles rising in a vertical channel. *J Fluid Mech*. 2001;429:307–342.
30. Spelt PDM, Sangani AS. Properties and averaged equations for flows of bubbly liquids. *Appl Sci Res*. 1998;58:337–386.
31. Ruzicka MC, Drahos J, Fialova M, Thomas NH. Effect of bubble column dimensions on flow regime transition. *Chem Eng Sci*. 2001;56(21–22):6117–6124.
32. Chen RC, Reese J; Fan LS. Flow structure in a three-dimensional bubble column and three-phase fluidized bed. *AIChE J*. 1994;40:1093–1104.
33. Bavarian F, Fan LS. Mechanism of hydraulic transport of a packed bed at the start-up of a three-phase fluidized bed. *Chem Eng Sci*. 1991;46(12):3081–3087.
34. Lau R, Cui Z, Fan LS. Liquid entrainment in high-pressure bubble columns. *Ind Eng Chem Res*. 2005;44:3776–3782.
35. Mudde RF, Saito T. Hydrodynamical similarities between bubble column and bubbly pipe flow. *J Fluid Mech*. 2001;437:203–228.
36. Clark NN, Atkinson CM, Flemmer RLC. Turbulent circulation in bubble columns. *AIChE J*. 1987;33:515–518.
37. Tomiyama A, Tamai H, Zun I, Hosokawa S. Transverse migration of single bubbles in simple shear flows. *Chem Eng Sci*. 2002;57;11:1849–1858.
38. Hamielec AE, Storey SH, Whitehead JH. Viscous flow around spheres at intermediate Reynolds' numbers. *Can J Chem Eng*. 1963;41:246–251.
39. Clift R, Grace JR, Weber ME. Bubbles, Drops and Particles. New York: Academic Press, 1978.
40. Tomiyama A. Struggle with computational bubble dynamics. In: *Third International Conference on Multiphase Flow*, ICMF' 98, Lyon, France, June 8–12. 1998.
41. Deckwer WD. Bubblecolumn Reactors. Chichester: Wiley, 1992:155–210.
42. Kastanek F, Zahradnik J, Kratochvil J, Cermak J. Chemical Reactors for Gas–Liquid Systems. Chichester: E. Horwood, 1993.
43. Molerus O. Principles of Flow in Disperse Systems. London: Chapman & Hall, 1993.
44. Kulkarni AA, Joshi JB, Ramkrishna D. Determination of bubble size distributions in bubble columns using LDA. *AIChE J*. 2004;50(12):3068–3084.
45. Mena PC, Ruzicka MC, Rocha FA, Teixeira JA. Drahos J. Effect of solids on homogeneous–heterogeneous flow regime transition in bubble columns. *Chem Eng Sci*. 2005;(60)22:6013–6026.
46. Ruzicka MC, Thomas NH. Buoyancy-driven instability of bubbly layers: analogy with thermal convection. *Int J Multiphase Flow*. 2003;29(2):249–270.
47. Loth E, Taeibi-Rahni M, Tryggvason G. Deformable bubbles in a free shear layer. *Int J Multiphase Flow*. 1997;23(5):977–1001.
48. Lucas D, Tomiyama A. On the role of the lateral lift force in polydispersed bubbly flows. *Int J Multiphase Flow*. 2011;37(9):1178–1190.
49. Lucas D, Prasser HM, Manera A. Influence of the lift force on the stability of a bubble column. *Chem Eng Sci*. 2005;60(13):3609–3619.
50. Burns AD, Frank T, Hamill I, Shi JM. The favre averaged drag model for turbulence dispersion in Eulerian multiphase flows. In: Fifth International Conference on Multiphase Flow, ICMF-2004. Japan: Yokohama, 2004:392.
51. Bluemink JJ, Lohse D, Prosperetti A, Van Wijngaarden L. Drag and lift forces on particles in a rotating flow. *J Fluid Mech*. 2010;643:1–31.
52. Ozbay H. Introduction to Feedback Control Theory. Boca Raton, FL: CRC Press, 1999. ISBN 084931867X.
53. Sato YT, Sadatomi M, Sekoguchi K. Momentum and heat transfer in two-phase bubble flow-I. *Int J Multiphase Flow*. 1981;7:167–177.

*Manuscript received Jun. 17, 2012, and revision received Dec. 14, 2013.*